



Contents lists available at ScienceDirect

International Journal of Applied Earth Observation and Geoinformation

journal homepage: www.elsevier.com/locate/jag



Real-time automated forest field inventory using a compact low-cost helmet-based laser scanning system

Jianping Li ^{a,b}, Bisheng Yang ^{a,*}, Yandi Yang ^a, Xin Zhao ^a, Youqi Liao ^a, Ningning Zhu ^a, Wenxia Dai ^c, Rundong Liu ^d, Ruibo Chen ^d, Zhen Dong ^a

^a State Key Laboratory of Information Engineering in Surveying, Mapping and Remote Sensing, Wuhan University, Wuhan, 430079, China

^b School of Electrical and Electronic Engineering, Nanyang Technological University, 50 Nanyang Avenue, 639798, Singapore

^c School of Geography and Information Engineering, China University of Geosciences (Wuhan), Wuhan 430074, China

^d Guangxi Zhuang Autonomous Region Remote Sensing Institute of Nature Resources, Nanning 530201, China



ARTICLE INFO

Keywords:

Point Cloud
Wearable laser scanning
Low-cost
Real-time forest inventory
Individual tree parameter

ABSTRACT

Forest field inventory plays a crucial role in forestry management and the estimation of carbon circular economy, as it provides information on forest parameters, assesses carbon storage, and identifies the impact factors of ecological change. Terrestrial Laser Scanning (TLS) and Mobile Mapping Systems (MMS) are commonly used for forest field inventory, but they are unable to verify the inventory results in real time. With real-time forest inventory, forestry workers can immediately verify if all trees have been correctly extracted without requiring expertise in point clouds. The advances of miniaturized, low-cost 3D sensors (such as solid-state laser scanners and Inertial Measurement Units [IMUs]) and edge computing units have made it possible to achieve real-time forest inventory using a compact, low-cost helmet. To this end, this paper presents a real-time automated forest field inventory method, which is validated on a compact, low-cost helmet-based laser scanning system. Firstly, a Fast Candidate Tree Detection (FCTD) approach is proposed to identify individual trees as candidates by utilizing a novel 2D corner detection technique based on point cloud projection, taking into account point density and geometry features. Secondly, a Spatiotemporal Consistency-based Tree Parameter Estimation (SCTPE) method is proposed to estimate the tree parameters by considering both the current submap and submaps that have been scanned in real-time. The proposed method was tested in three typical forest areas in Wuhan, China, where the main tree species present include Sapindaceae, dawn redwoods, and Platycladus. The results showed that the proposed method achieves high accuracy in tree detection (*recall* = 0.97, *precision* = 0.94, *F* = 0.96). The average error and root-mean-square error (RMSE) of DBH are 0.033 m and 0.038 m, which outperforms the existing one-circle fitting model. The average error and RMSE of tree height are 0.231 m and 0.294 m. Overall, these results demonstrate the high potential of the helmet-based laser scanning system for real-time forest field inventory.

1. Introduction

Forests occupy approximately one-third of the Earth's land surface and are vital to ecological changes and the global carbon cycle (Mitchard, 2018). Accurate estimation of forest parameters can reveal the influencing factors of ecological changes (Wang et al., 2019) and assess carbon storage (Xiao et al., 2019), providing valuable information for forest management, forestry policy formulation (Liu et al., 2018) and the circular economy of carbon (Näyhä, 2019).

Forest field inventory is a key tool for surveying forest resources by

counting tree parameters in sample plots and summarizing the statistics (Hyypä et al., 2020). Traditional forest field inventory methods, which involve measuring the diameter at breast height (DBH) of all trees in the sample plot and the height of a few trees, are labor-intensive and have low operational efficiency (Lei et al., 2009). With the advancement of laser scanning technology, Terrestrial Laser Scanning (TLS) is widely used to acquire high-precision point clouds for forest field inventory (Liang et al., 2016). Vehicle-borne Mobile Mapping Systems (MMS), equipped with laser scanners and a positioning and orientation system (POS), can also collect point clouds in forests, offering improved point

* Corresponding author.

E-mail addresses: jianping.li@ntu.edu.sg (J. Li), bshyang@whu.edu.cn (B. Yang).

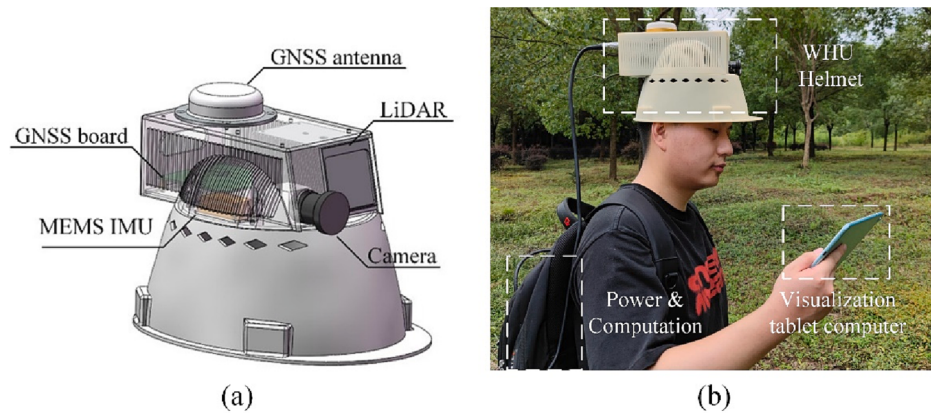


Fig. 1. Hardware of the helmet system. (a) Sensor configuration of the helmet; (b) Forest inventory using the helmet system.

cloud acquisition efficiency compared to TLS (Bienert et al., 2018; Kuželka et al., 2022). However, the quality of point clouds obtained by MMS is not guaranteed in dense forests where global navigation satellite system (GNSS) signals are not available (Kukko et al., 2017). To overcome this challenge, Simultaneous Localization and Mapping (SLAM) methods are used to match subsequent laser frames and limit the drift of the POS in dense forests, leading to high-precision point clouds (Qian et al., 2016). As a result, SLAM systems have been successfully used for forest field inventory in GNSS-denied environments (Chudá et al., 2020; de Miguel-Díez et al., 2022; Su et al., 2020). The recent advances in miniaturized and low-cost 3D sensors, such as solid-state laser scanners and Micro-Electro-Mechanical System (MEMS) Inertial Measurement Units (IMUs), have enabled the integration of a SLAM systems into a compact helmet worn by forestry workers (GIMinternational, 2021; Li et al., 2022).

Besides lightweight and miniaturization, forest inventory equipment with real-time processing capability is also preferred (Fan et al., 2020). The real-time processing capability of this equipment allows the workers to concentrate on tree parameters without having to have a deep background in point clouds and related software. In this way, real-time inventory of forest sample plots can be carried out with ease, avoiding

post-processing, reducing the operational difficulty, and improving the timeliness of data collection. The workers can also check on-site if all the trees have been extracted, reducing the possibility of missed or incorrect data and the need for repeated trips to the sample plot (Chen et al., 2020; Proudman et al., 2022). However, most of the existing forest field inventory methods are divided into two steps: point cloud acquisition and post-processed tree parameter estimation (Kükenbrink et al., 2022; Liang et al., 2018b; Mokroš et al., 2021).

Realizing real-time automated forest field inventory on a compact wearable device requires tree parameter estimation being performed on an edge-computing unit. The limited computing resources of wearable laser scanning systems, such as Intel NUC or Nvidia Xavier, pose a challenge for most existing tree detection and parameter estimation algorithms that are computationally intensive and cannot perform in real time. For example, the minimum-cut-based method (Yang et al., 2016) and mean-shift-based method (Dai et al., 2018), which use point-by-point feature calculation and global iterative optimization, are difficult to perform in real time on low-power edge computing units. Although recent studies have attempted to address this challenge by using Euclidean clustering (Proudman et al., 2022) or deep learning (Chen et al., 2020), there are still limitations, such as difficulty in identifying single trees in complex dense forests or limited generalization between data collected by different sensors and in various forest environments. Although transfer learning (Zhu et al., 2020) has improved the generalization of deep learning networks between data collected by different sensors and in various forest environments, the distribution gap between the training and evaluation datasets is still hard to mitigate. Big effort of manual labelling for the new dataset and new type of laser scanner is usually required for the deep learning network (Behley et al., 2021). Moreover, point cloud data from multiple laser frames may be missing information about individual trees, making it difficult to ensure the consistency of results from multiple laser frames. Therefore, developing a real-time forest field inventory system remains a challenging task.

The goal of this paper is to develop a real-time automated forest field inventory system using a compact helmet-based laser scanning system. The main contributions are two-fold:

(1) A Fast Candidate Tree Detection (FCTD) algorithm is proposed to identify the candidate trunk positions in the point cloud submap. It uses a novel 2D corner detection approach based on point density and geometry features, which allows for real-time performance on edge computing units.

(2) A spatiotemporal consistency-based tree parameter estimation (SCTPE) is proposed to estimate the tree parameters considering the current point cloud submap and point cloud submaps that have been scanned in real time. It overcomes the problem of missing data in the current submap due to occlusion. Specifically, SCTPE uses spatial consistency validation to eliminate incorrect tree candidates, followed by a

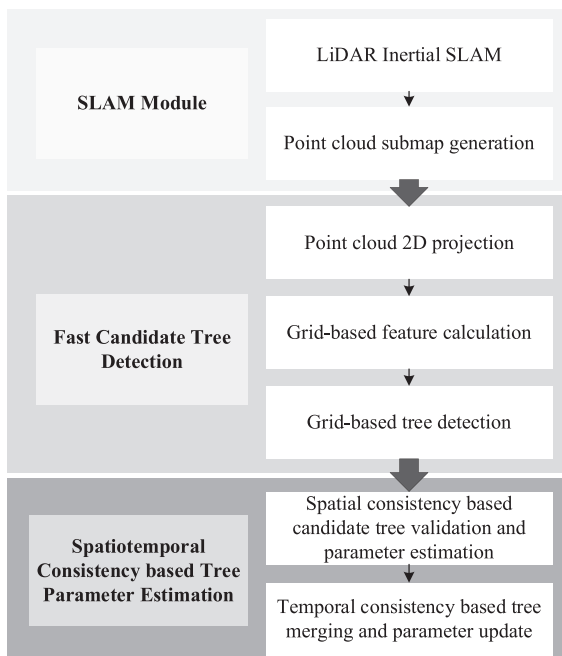


Fig. 2. Workflow of the real-time automated forest inventory.

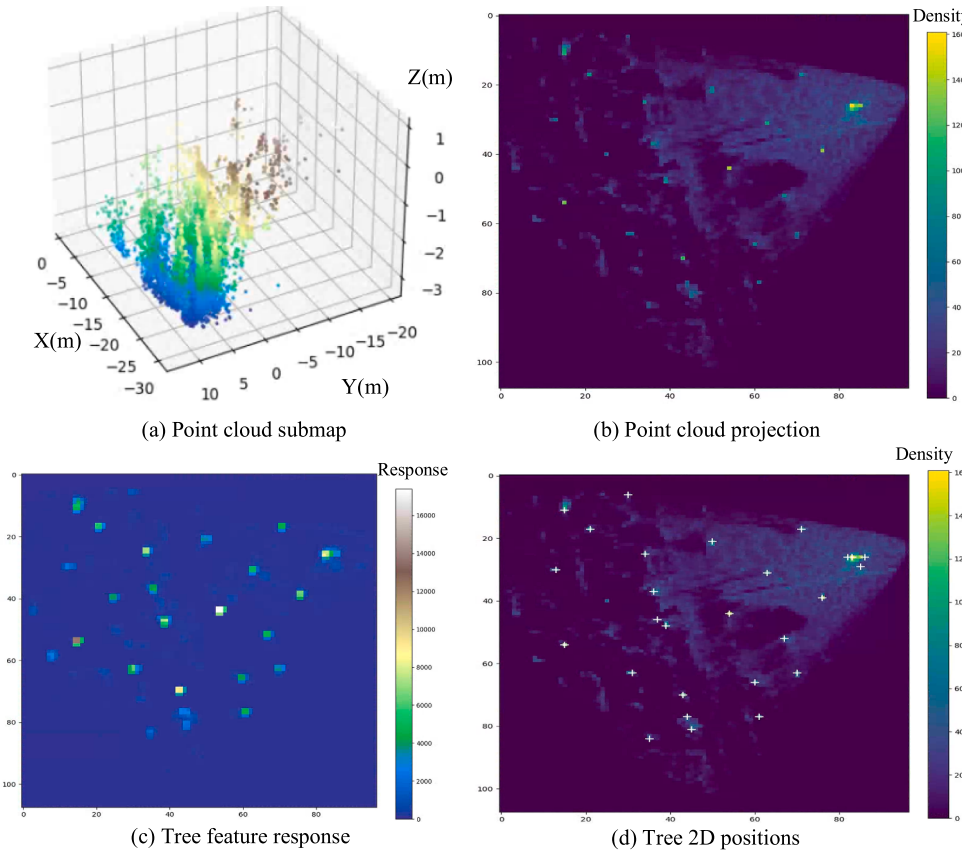


Fig. 3. Illustration of Fast Candidate Tree Detection (FCTD).

global consistent tree parameter estimation using a temporal consistency-based parameter update.

The rest of the paper is structured as follows: In Section 2, the proposed real-time automated forest field inventory system is described in detail. The experimental results and validation of the proposed method are presented in Section 3. Finally, a discussion of the results is given and the conclusions are drawn.

2. Method

2.1. System overview

For an easy description of the proposed method, the configuration of the hardware is first detailed in this section. The compact helmet laser scanning system, named WHU-Helmet (Li et al., 2022), is shown in Fig. 1 (a). Multiple sensors are integrated into a helmet, which includes a GNSS receiver (Novatel OEM-719), solid laser scanner (LiVOX-Avia (livoxtech, 2023)), IMU (Honeywell I300), and a global shutter camera. The multi-sensor time synchronization is fulfilled using a hardware circuit (Li et al., 2019) to ensure the accuracy of the time reference. The total weight of the helmet system is 1.5 kg. The operation of the WHU-Helmet is shown in Fig. 1(b). Using the tablet computer, an operator can check inventory status and progress in real time.

Using the multi-sensory data obtained by WHU-Helmet in real time, the workflow of real-time automated forest inventory proposed in this paper is shown in Fig. 2. Three main modules, SLAM module, fast candidate tree detection (FCTD), and spatiotemporal consistency-based tree parameter estimation (SCTPE), are involved in the workflow. Fast LiDAR-Inertial Odometry (Fast-LIO) (Xu et al., 2022) is used as the SLAM framework to fuse laser and IMU data for pose estimation. Point clouds collected in 2 s by the SLAM module are treated as a point cloud submap and sent to the sequent module for tree detection. We use 2 s for

accumulating enough laser scanning point cloud while balancing the real-time visualization on the tablet computer according to our experience. Then, the proposed FCTD runs at 0.5 Hz to obtain the candidate trees. Finally, SCTPE also runs at 0.5 Hz to verify the spatial consistency of the candidate trees and update the parameters between current submap and submaps just scanned for temporal consistency. The main contributions of this work, FCTD and SCTPE are described in detail as follows.

2.2. Fast candidate tree detection (FCTD)

FCTD is proposed to detect individual trees from the point cloud submap. First, the input point cloud submap (Fig. 3(a)) is projected on a 2D grid with a grid size of S_{Grid2D} . A small value of S_{Grid2D} means a high resolution of the projected 2D grid, leading to high sensitivity to noise and false detection. On the contrary, a big value of S_{Grid2D} leads to a big error in tree positions and low detection precision. S_{Grid2D} is set to 0.4 m in the experiment. Meanwhile, the lowest height $H_{min}(x,y)$ and the highest height $H_{max}(x,y)$ is calculated for each 2D grid (x,y) . The ground $H_{ground}(x,y)$ of the grid is calculated by selecting the lowest height of the neighborhood with a radius of $S_{NeighborGround}$. As the ground point may not be scanned in a local grid far from the helmet system, the tree point may be taken as the ground point, resulting in an elevation estimation error. Thus, the lowest height of the neighborhood with a radius $S_{NeighborGround}$ is considered. However, setting $S_{NeighborGround}$ too large will cause the elevation calculation too smooth, which is not suitable for areas with large elevation changes. $S_{NeighborGround}$ is set to 2 m in the experiment. To avoid the influence of ground points and crown points when extracting the tree trunk position, the points within the height range of $[H_{ground}(x,y) + 0.1, H_{ground}(x,y) + H_{DBH}]$ are projected and used to calculate the point size within a grid, namely the density $I(x,y)$. According to the definition that DBH is the diameter of the trunk at the height of 1.3

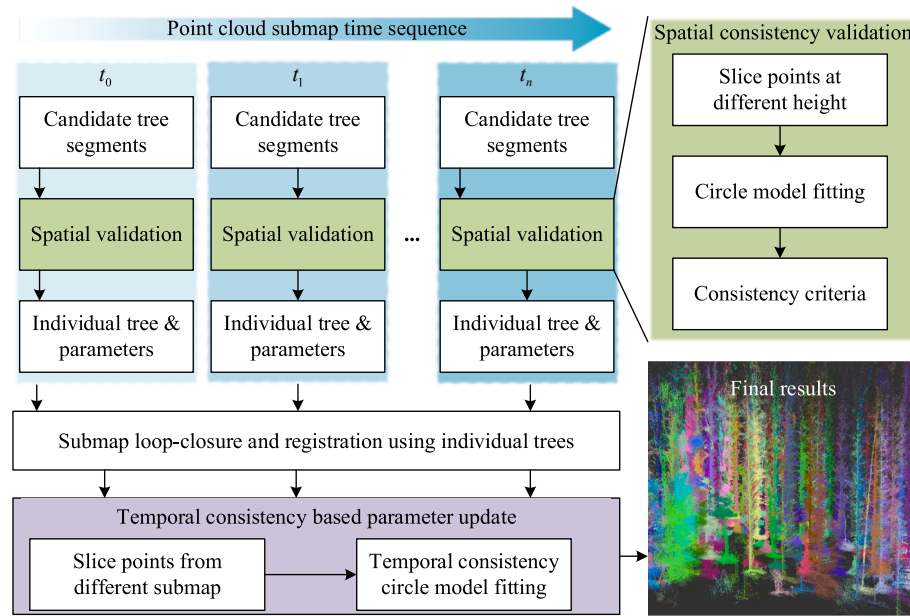


Fig. 4. Illustration of Spatiotemporal Consistency-based Tree Parameter Estimation (SCTPE).

m , $H_{DBH} = 1.3m$. It can be found that the tree trunk presents a local extremum in the point density map as shown in Fig. 3(b). Therefore, the density changes in the local window of $I(x, y)$ is used as an indicator of the tree trunk. Let the change in the local window of $I(x, y)$, $E(x, y)$ is calculated by:

$$E(x, y) = \sum_{u \in [-1, 1]} \sum_{v \in [-1, 1]} G(x, y) \times [I(x + u, y + v) - I(x, y)]^2$$

where, $G(x, y)$ is the Gaussian kernel for noise smoothing (Hsiao et al., 2010). To analyze the numerical characteristics of $E(x, y)$, Eq. is rewritten as follows:

$$\begin{aligned} E(x, y) &\approx \sum_{u \in [-1, 1]} \sum_{v \in [-1, 1]} G(x, y) \times \left[\frac{\partial I}{\partial x} u + \frac{\partial I}{\partial y} v \right]^2 \\ &= [u, v] \underbrace{\sum_{u \in [-1, 1]} \sum_{v \in [-1, 1]} G(x, y) \times \begin{bmatrix} \left(\frac{\partial I}{\partial x} \right)^2 & \frac{\partial I^2}{\partial x \partial y} \\ \frac{\partial I^2}{\partial x \partial y} & \left(\frac{\partial I}{\partial y} \right)^2 \end{bmatrix}}_M \begin{bmatrix} u \\ v \end{bmatrix} \end{aligned}$$

In the above formula, the matrix M describes the feature of point density change in the local window. The local window size has nearly the same impact as the 2D grid size S_{Grid2D} , which controls the local detection range. But if we use a larger window size, it will use more computation resources as illustrated in Eq. (2). In the consideration of real-time performance, we set the window size as 1, and adjust the local detection range by changing the 2D grid size S_{Grid2D} . The eigenvalue (λ_1, λ_2) of M is obtained using singular value decomposition (SVD). If both of λ_1 and λ_2 are small, it indicates that the point cloud density changes gently in the local window and there is no tree trunk in the local window. If both of λ_1 and λ_2 are large, it indicates that there is an extreme point in the local window, and there is a candidate tree trunk to be selected. Thus, the minimum eigenvalue of M at position (x, y) is treated as the tree trunk response value, and written by $Response(x, y)$.

To sum up, the coordinate (x, y) that meets the following conditions is selected as the candidate tree trunk: (1) $Response(x, y) > \lambda_{min}$, which indicates point intensity at (x, y) is the local extreme value and determines the criteria for indicating a corner point, which is set to 1000 in the experiment; (2) $Response(x, y)$ is the maximum value in the radius of

$S_{NeighborResponse}$, which is used to identify the maximum value within a certain range to select the best trunk position and set to 1 m in the experiment; (3) $(H_{max}(x, y) - H_{ground}(x, y)) > H_{DBH}$, which eliminates low bush. If the coordinate (x, y) is detected as the tree trunk, taking the coordinate (x, y) as the center, 3D point clouds in the radius of $S_{NeighborResponse}$ are gathered as a tree segment for the following processing.

2.3. Spatiotemporal Consistency-based tree parameter estimation (SCTPE)

Taking the candidate tree segments from FCTD as input, the proposed SCTPE selects the valid candidate tree segments based on spatial consistency and obtains temporal consistent tree parameters, whose workflow is shown in Fig. 4. There are two key parts in SCTPE for validation and parameter estimation: **Spatial consistency-based validation** (Section 2.3.1) verifies the candidate trees in a point cloud submap; **Temporal consistency-based parameter update** (Section 2.3.2) estimates the tree parameters of the same tree observed from different point cloud submap.

2.3.1. Spatial consistency-based validation

First, for the candidate tree segments obtained at time t_n , points cross sections at height of 1.3 m, 1.5 m, and 1.7 m are extracted. Then, circle fitting is performed in cross sections of random sample consensus (RANSAC) (Derpanis, 2010). Let the m points in a cross-section be $\{(x_0, y_0), (x_1, y_1), \dots, (x_m, y_m)\}$, the equation of circle center and radius are c_x, c_y and R is written by Eq.. The equation is solved by the least square method as Eq.. According to the assumption that the radii of the tree trunk at different heights change slowly, the current candidate tree segment is validated by checking the difference between radii at 1.3 m, 1.5 m, and 1.7 m. In the experiment, the average error of the DBH estimation using our system is about 0.03 m. We use 0.1 m (3 sigmas) to filter out the outliers. Finally, the DBH is calculated.

$$\underbrace{\begin{bmatrix} -2x_0 & -2y_0 & -1 \\ \vdots & \vdots & \vdots \\ -2x_m & -2y_m & -1 \end{bmatrix}}_A \begin{bmatrix} c_x \\ c_y \\ R \end{bmatrix} + \underbrace{\begin{bmatrix} x_0^2 + y_0^2 \\ \vdots \\ x_m^2 + y_m^2 \end{bmatrix}}_b = 0_{m \times 1}$$

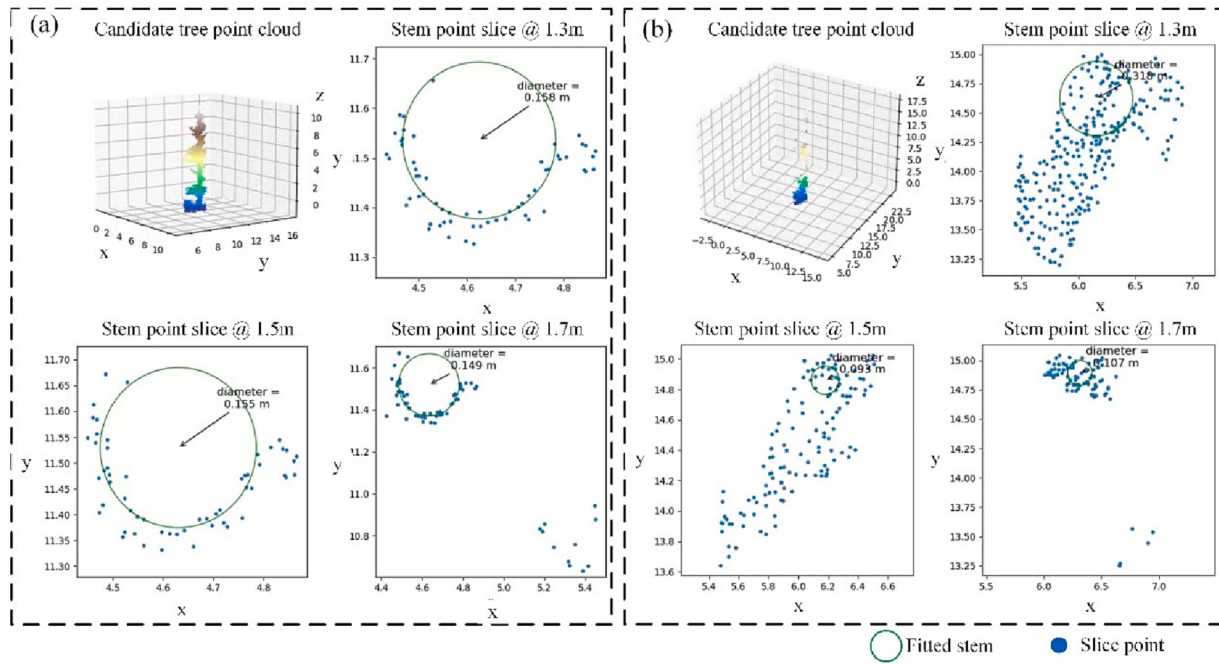


Fig. 5. Spatial consistency-based candidate tree validation. (a) Correct tree candidate; (b) Incorrect tree candidate.

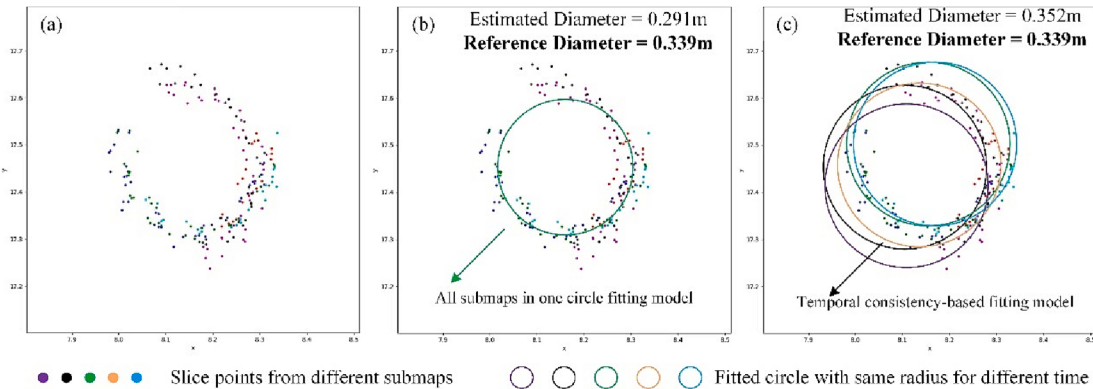


Fig. 6. Temporal consistency-based diameter parameter update. (a) Registered individual tree point slices from multiple submaps. (b) Circle fitting. (c) Temporal consistency-based circle fitting.

$$\begin{bmatrix} c_x \\ c_y \\ R \end{bmatrix} = -(A^\top A)^{-1} A^\top b$$

Fig. 5 indicates two typical examples of spatial consistency-based validation. The points cross sections at height of 1.3 m, 1.5 m, and 1.7 m are extracted from the candidate tree point cloud in Fig. 5 (a). After utilizing RANSAC and circle fitting, the resulting diameters are 0.158 m, 0.155 m, and 0.149 m respectively. Since the differences between adjacent diameters are 0.03 m and 0.06 m, both of which are less than 0.1 m, it is judged as a valid tree trunk. However, in Fig. 5 (b), the differences between adjacent diameters of the candidate tree points are greater than 0.1 m, which indicates an invalid candidate.

2.3.2. Temporal consistency-based diameter parameter update

The inconsistency of LiDAR SLAM in complex forests is still a challenging task for the SLAM community (Pierzchala et al., 2018). The FAST-LIO (Xu et al., 2022) used in the system is the SOTA SLAM method. As this is a common unsolved problem for SLAM, the proposed method achieves the real-time forest inventory using another strategy. Using the

individual tree trunk as registration primitives for pose graph optimization, point cloud submaps are first registered to correct trajectory error and mitigate the cumulated SLAM drift (Chen et al., 2020). More specifically, for each tree trunk in the current point cloud submap, we search the nearest tree trunk in existing point cloud submaps as the corresponding match. Then a pose graph optimization is constructed using the corresponding matches for adjusting the poses for all. The cross-section for the same individual tree observed from multiple submaps is registered as shown in Fig. 6 (a). From Fig. 6 (a), it can be found that it is difficult to completely correct the SLAM error by pose graph optimization due to the deformation in the submaps from SLAM (Yang and Li, 2022). The points from different submaps tend to cluster together because of the registration error. If the circular fitting is performed directly on the registered cross-section, the DBH estimation error will increase as shown in Fig. 6 (b). The distribution of the color points is not the real case but with SLAM drift. Even, the circle fitted to all submaps (with drift) but has a large error. Therefore, temporary consistency-based circle fitting is utilized according to the fact that the estimated DBH of one tree trunk observed from different point cloud submaps should be the same. Because in a short time during the data collection,

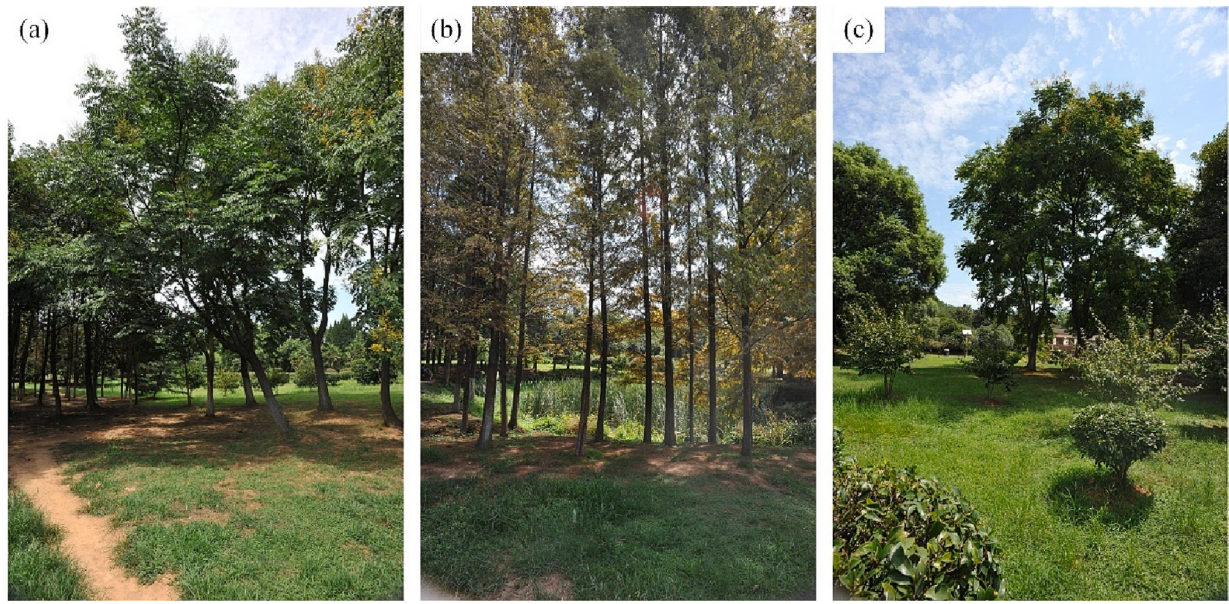


Fig. 7. Main planted tree species in the study area. (a) Sapindaceae (*Koelreuteria paniculata*); (b) dawn redwood (*Metasequoia glyptostroboides*); (c) *Platycladus* (*Platycladus orientalis*).

the geometry of the tree stems is not changed.

Let the cross-section points for one tree observed at time sequence t_0, t_1, \dots, t_n are $\{(x_{t_0}^0, y_{t_0}^0), (x_{t_0}^1, y_{t_0}^1), \dots, (x_{t_0}^{m_{t_0}}, y_{t_0}^{m_{t_0}})\}, \dots, \{(x_{t_n}^0, y_{t_n}^0), (x_{t_n}^1, y_{t_n}^1), \dots, (x_{t_n}^{m_{t_n}}, y_{t_n}^{m_{t_n}})\}$, where m_{t_n} is the number of points observed at time t_n . Due to the deformation in the submaps from SLAM, let the center offsets of the tree trunk in different submaps are $(c_{t_0}^x, c_{t_0}^y), (c_{t_1}^x, c_{t_1}^y), \dots, (c_{t_n}^x, c_{t_n}^y)$. The radius of the tree trunk is R . Then we could infer Eq.. Eq. can also be solved using the least square method so that the DBH parameter can be updated as shown in Fig. 6 (c).

(114.43° N, 30.53° E), Wuhan City, Hubei Province, China. The main planted tree species in the study area include Sapindaceae (*Koelreuteria paniculata*), dawn redwood (*Metasequoia glyptostroboides*), and *Platycladus* (*Platycladus orientalis*). The photos taken from three sample plots are shown in Fig. 7. Nine sample plots were evenly selected from the study sites. Each sample plot is a circular area with a radius of 15 m. The statistics of the sample plots are listed in Table 1.

The TLS (Riegler VZ 400) is used to collect the reference point clouds as shown in Fig. 8 (a). To achieve a full scanning of the trees in the sample plots, at least 3 individual TLS scans are collected for each sample plot. Then the individual scans from different scan positions are manually registered using CloudCompare. Using CloudCompare, we first selected significant corresponding feature points from different TLS point clouds for the coarse registration. Then the fine registration based on ICP was

$$\begin{bmatrix} -2x_{t_0}^0 & -2y_{t_0}^0 & 0 & 0 & \cdots & 0 & 0 & 1 \\ \vdots & \vdots & \vdots & \vdots & \ddots & \vdots & \vdots & \vdots \\ -2x_{t_0}^{m_{t_0}} & -2y_{t_0}^{m_{t_0}} & 0 & 0 & \cdots & 0 & 0 & 1 \\ 0 & 0 & -2x_{t_1}^0 & -2y_{t_1}^0 & \cdots & 0 & 0 & 1 \\ \vdots & \vdots & \vdots & \vdots & \ddots & \vdots & \vdots & \vdots \\ 0 & 0 & -2x_{t_1}^{m_{t_1}} & -2y_{t_1}^{m_{t_1}} & \cdots & 0 & 0 & 1 \\ \vdots & \vdots & \vdots & \vdots & \ddots & \vdots & \vdots & \vdots \\ 0 & 0 & 0 & 0 & \cdots & -2x_{t_n}^{m_{t_0}} & -2y_{t_n}^{m_{t_0}} & 1 \\ \vdots & \vdots & \vdots & \vdots & \ddots & \vdots & \vdots & \vdots \\ 0 & 0 & 0 & 0 & \cdots & -2x_{t_n}^{m_{t_n}} & -2y_{t_n}^{m_{t_n}} & 1 \end{bmatrix} \begin{bmatrix} c_{t_0}^x \\ c_{t_0}^y \\ c_{t_1}^x \\ c_{t_1}^y \\ \vdots \\ c_{t_n}^x \\ c_{t_n}^y \\ R \end{bmatrix} + \begin{bmatrix} (x_{t_0}^0)^2 + (y_{t_0}^0)^2 \\ \vdots \\ (x_{t_0}^{m_{t_0}})^2 + (y_{t_0}^{m_{t_0}})^2 \\ (x_{t_1}^0)^2 + (y_{t_1}^0)^2 \\ \vdots \\ (x_{t_1}^{m_{t_1}})^2 + (y_{t_1}^{m_{t_1}})^2 \\ \vdots \\ (x_{t_n}^0)^2 + (y_{t_n}^0)^2 \\ \vdots \\ (x_{t_n}^{m_{t_n}})^2 + (y_{t_n}^{m_{t_n}})^2 \end{bmatrix} = 0_{(m_{t_0}+m_{t_1}+\cdots+m_{t_n}) \times 1}$$

3. Experiments and results

3.1. Study area and ground truth dataset

The study area is located in Ma'an Mountain Forest

performed to achieve accurate registration. The accuracy of the above registration process in a forest environment is within the centimeter level, which is sufficient for forest inventory (Dong et al., 2020). The point cloud registration error is within 0.01 m by analyzing the closest points from multiple scans using CloudCompare. The registered dense

Table 1

Statistical summary of sample plot attributes.

Sample plot ID	Sample plot density (stems/ha)	DBH (m)				Tree height (m)			
		Min	Max	Mean	STD	Min	Max	Mean	STD
1	254.78	0.28	0.98	0.49	0.21	1.70	9.45	7.79	1.81
2	283.09	0.39	0.68	0.50	0.07	5.12	9.45	8.15	1.05
3	184.01	0.35	0.54	0.44	0.07	3.71	9.77	8.61	1.53
4	198.16	0.36	0.66	0.50	0.11	1.69	9.36	7.94	1.92
5	297.24	0.10	0.56	0.34	0.56	2.90	9.54	6.67	2.30
6	240.62	0.20	0.70	0.53	0.12	2.36	11.60	7.87	3.83
7	552.02	0.18	0.52	0.30	0.08	16.68	25.45	18.16	1.17
8	537.86	0.20	0.49	0.32	0.08	14.15	18.33	17.80	0.66
9	679.41	0.18	0.57	0.31	0.10	6.06	18.22	15.15	3.90

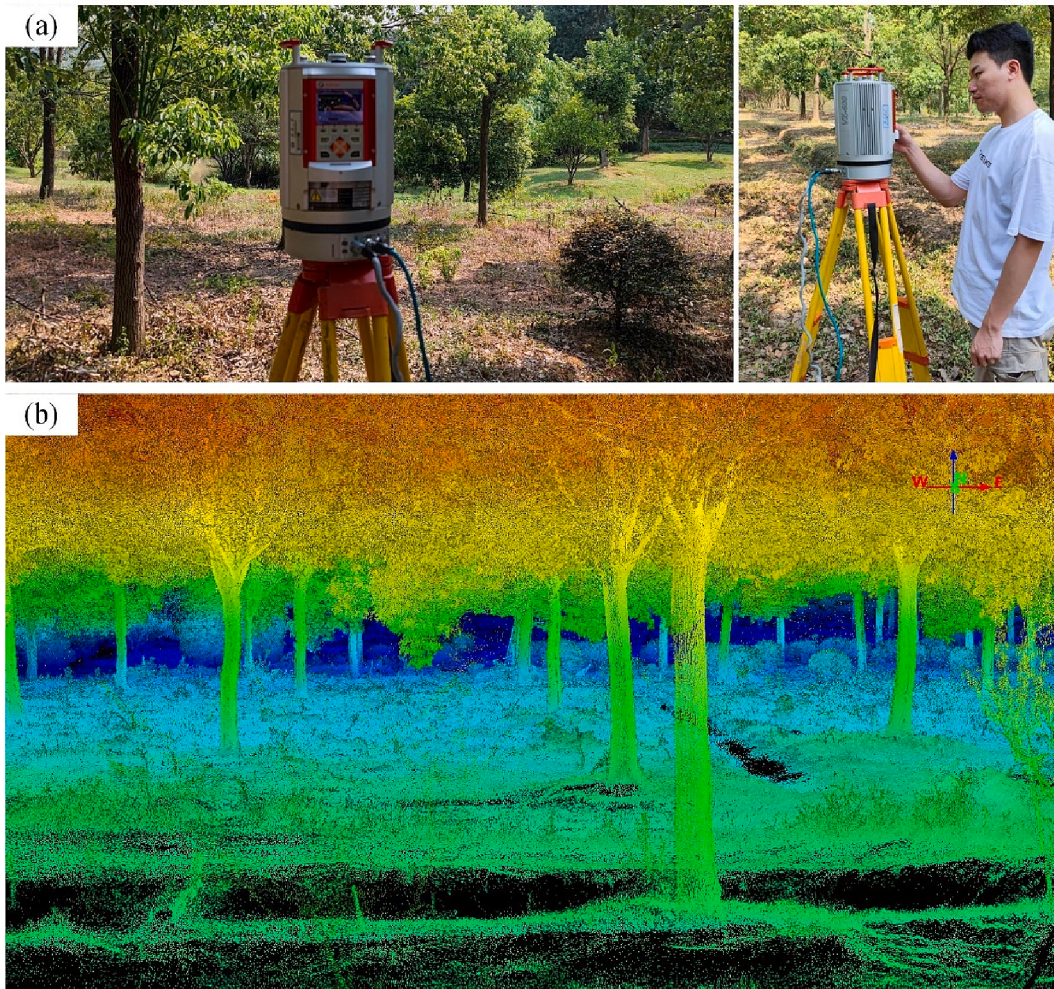


Fig. 8. Reference point cloud collected by terrestrial laser scanning (TLS). (a) Field 3D point cloud collection using Riegl VZ 400. (b) The registered point cloud using multiple scans from different scan positions for complete coverage of the trees in the sample plot.

TLS point cloud for a sample plot is shown in Fig. 8 (b). The dense full coverage TLS point cloud could provide an accurate data basis for the following tree parameters extraction (Liang et al., 2018a).

Using the dense fully overaged TLS point cloud, the ground truth individual tree parameters, including trunk position, DBH, and tree height are surveyed manually in the TLS point clouds via the software Point2Model (Point2Model, 2023) developed by our previous work. The manual tree survey process mainly consists of two steps. First, a tree position and crown diameter are selected as shown in Fig. 9 (a). Then, the point cloud for the currently selected tree is visualized from top, front, and side views. Meanwhile, the tree stem is fitted automatically and shown in the software for the manual check as shown in Fig. 9 (b). If the stem fitting result and parameters are correct after check, they will

be saved as the ground truth data. The accuracy of DBH and tree height of part of our ground truth (10 trees for each study site) are validated using a measuring tape and a total station (Yan et al., 2012). The accuracy of ground truth DBH is within 0.02 m. The accuracy of ground truth tree height is within 0.12 m. The reference point cloud and ground truth for the nine sample plots are shown in Fig. 10.

3.2. Helmet dataset collection

The operator wearing WHU-Helmet walks in the forest at about the speed of 1–1.5 m/s. The visualization of the real-time collected point cloud and trajectory in three study sites using the helmet system is shown in Fig. 11. The whole walking trajectories of the operator and

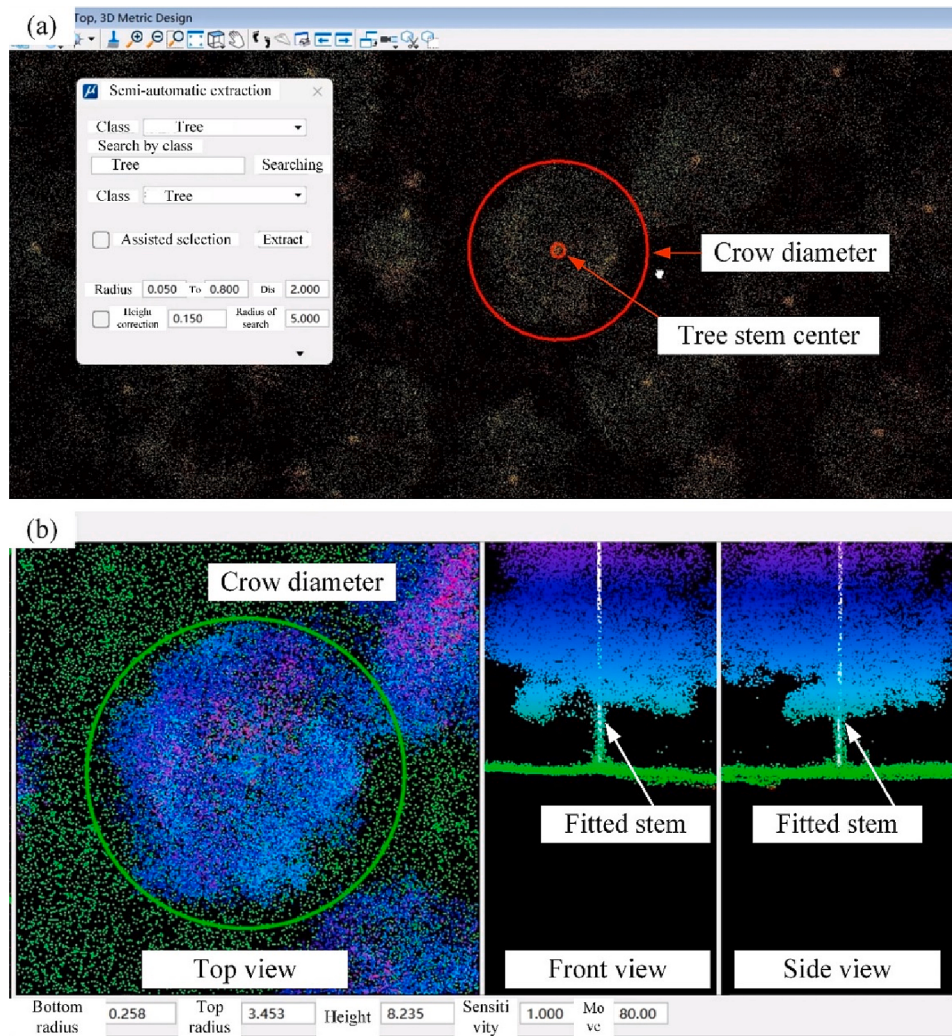


Fig. 9. Manual labeling of the tree parameters using TLS point clouds. (a) Manually select the tree stem and crow diameter from the top view. (b) Manually adjust the fitted tree stem using three perspective views (top, front, and side views).

collected point cloud are illustrated in Fig. 12. The raw data of the helmet is logged using robot operating system (ROS) via rosbag¹ to evaluate the real-time performance of the proposed method. It takes about 4 min for collecting data in each sample plot.

3.3. Evaluation criteria

To evaluate the accuracy of the tree detection results, three commonly used indices, namely “recall”, “precision”, and “F-measure”, are adopted. “recall”, “precision”, and “F-measure” (Powers, 2020) are calculated as follows:

$$\text{recall} = \frac{TP}{TP + FN}$$

$$\text{precision} = \frac{TP}{TP + FP}$$

$$F\text{-measure} = \frac{2 \times \text{recall} \times \text{precision}}{\text{recall} + \text{precision}}$$

where TP (True Positive) is the number of individual trees detected correctly; FN (False Negative) is the number of individual trees that exist

but fail to be detected; FP is the number of wrong tree trunks that do not exist in the ground truth data. To evaluate the accuracy of the individual tree parameters estimated in real-time, the resulting parameters, DBH and tree height, are compared with ground truth data.

3.4. Parameters settings and sensitive analysis

The 2D grid size S_{Grid2D} (determining the resolution of the point cloud projection) and Eigen value judgment criteria λ_{min} (determining the criteria for indicating a corner point) have a high relationship, which are the most important parameters to be set in the proposed method. As shown in Fig. 13, tree feature response and detection results using different 2D grid sizes S_{Grid2D} with fine-tuned Eigen value judgment criteria λ_{min} are illustrated. From the visualization of change S_{Grid2D} , it can be observed that setting S_{Grid2D} a too small value (e.g., 0.2 m) leads to high sensitiveness to noise and false detection. On the contrary, a big value of S_{Grid2D} (e.g., 0.6 m) leads to a big error in tree positions and low detection precision. Thus, using the data in sample plot 1 for the parameter sensitivity analysis, the F-measure for tree detection results with different S_{Grid2D} and λ_{min} is plotted in Fig. 14, where $S_{Grid2D} = 0.4\text{m}$, $\lambda_{min} = 1000$ achieving the best performance.

The radius for ground calculation $S_{NeighborGround}$ is also an important parameter that should be set according to the study area, as the accuracy of elevation affects the calculation of tree height and DBH. If setting $S_{NeighborGround}$ too small, the ground point may not be scanned in a local

¹ <https://wiki.ros.org/rosbag>.

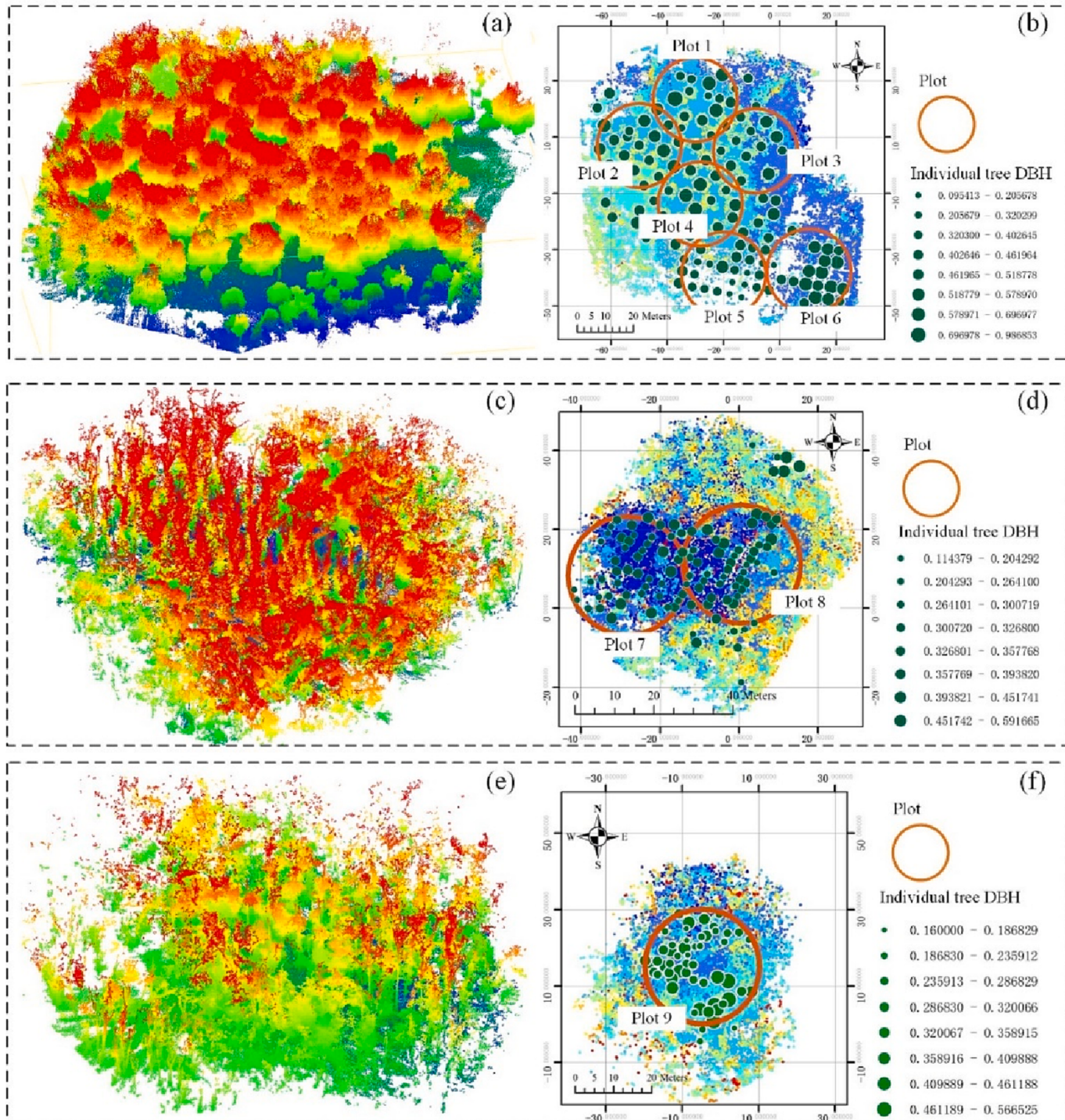


Fig. 10. Ground truth individual tree and parameter collected by terrestrial laser scanning (TLS) and labeled manually. (a), (b) Point cloud and ground truth of study site 1; (c), (d) Point cloud and ground truth of study site 2; (e), (f) Point cloud and ground truth of study site 3.

grid far from the helmet system, so the tree point may be taken as the ground point, resulting in an elevation estimation error. However, setting $S_{Neighborhood}$ too large will cause the elevation calculation too smooth, which is not suitable for areas with large elevation changes. To achieve the balance, we extract the Digital elevation model (DEM) of study site 1 using the TLS point cloud via cloth simulation filtering (CSF) (Zhang et al., 2016) and analyzed the elevation error with different $S_{Neighborhood}$ as shown in Fig. 15. From Fig. 15 (c), $S_{Neighborhood} = 2\text{m}$ achieve the best performance.

The other parameters used in the proposed method are relatively

easily and reasonably set. The radius of non-maximum suppression $S_{Neighborhood}$ is used to identify the maximum value within a certain range to select the best trunk position. $S_{Neighborhood}$ could be set according to the density of the trees. For example, in the study areas, there is no more than one tree within one-meter distance, so $S_{Neighborhood}$ can be set as 1 m. The effective scanning range of LiVOX is quite large, about 200 m, which leads to a low density of the point cloud far from the scanner. Therefore, minimum point density I_{min} is used to screen the 2D grid with too few point projections for effective detection.

The densities of the 9 sample plots from 3 study sites range from 180

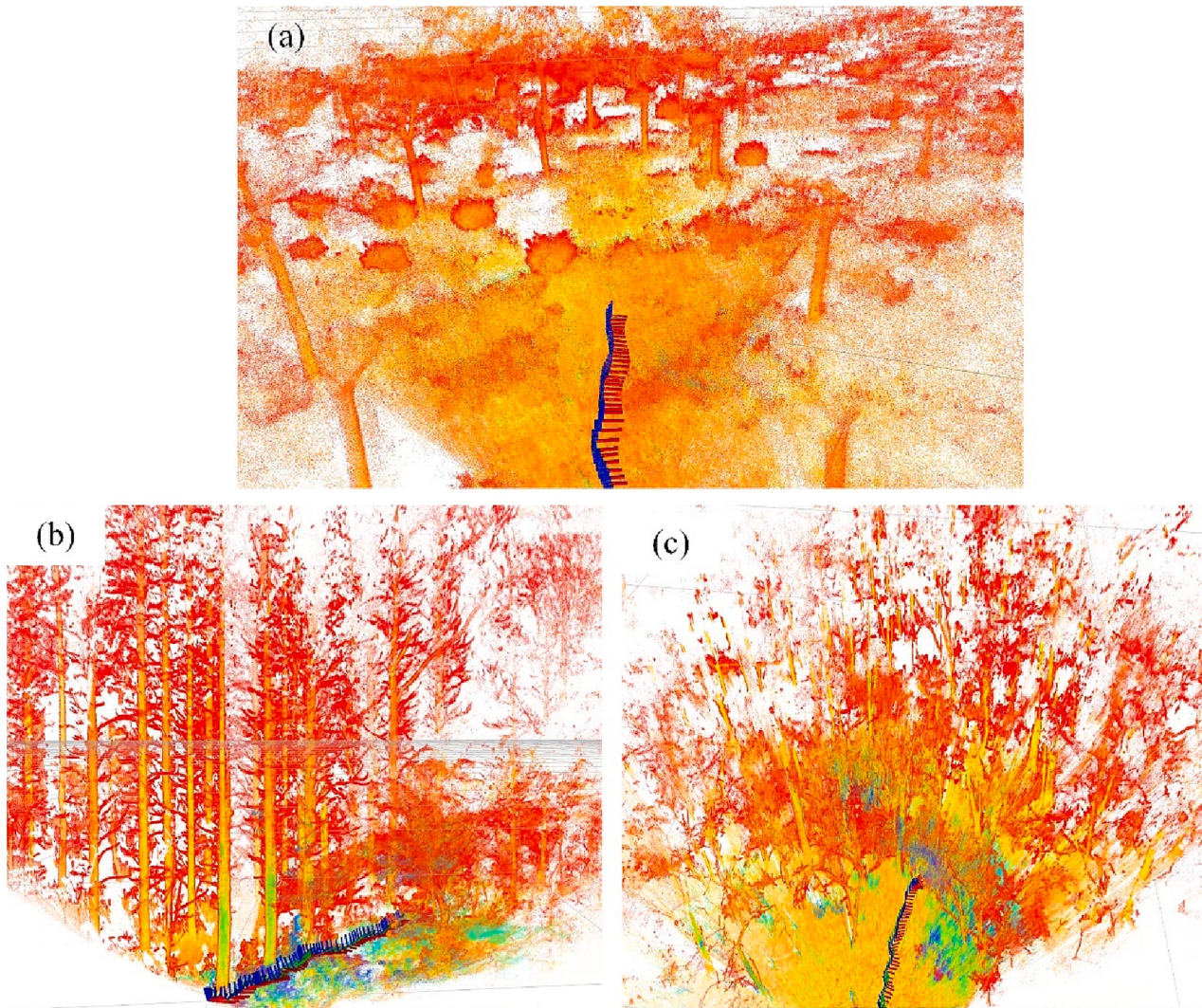


Fig. 11. Visualization of the real-time collected point cloud and trajectory using the helmet system in robot operating system (ROS). The point cloud is rendered according to the intensity. (a) Study site 1; (b) Study site 2; (c) Study site 3.

stems/ha to 680 stems/ha, which are all relatively sparse distributions. Thus, the parameters related to densities like 2D grid size S_{Grid2D} and Eigenvalue judgment criteria λ_{min} would be suitable for the three study sites. The radius for ground calculation $S_{NeighborGround}$ is related to the slope of the study sites. As the three study sites are all located in the relief area, $S_{NeighborGround}$ is suitable for all study sites. The radius of non-maximum suppression $S_{NeighborResponse}$ and min point density I_{min} is related to the point density. The walking speeds of the operator in the three study sites are all about $1 \sim 1.5$ m/s, they are suitable for the three study sites too. To sum up, we list the parameter settings used for the following experiments in Table 2.

3.5. Time performance

The proposed real-time forest inventory is performed on the Intel NUC edge-computing unit with 32 GB RAM, Intel Core i7-12700H Processor @ 4.7 GHz. The FCTD and SCTPE are implemented as independent ROS nodes and launched on the edge-computing unit at the same time along with the SLAM module. Table 3 lists the time performance of the FCTD and SCTPE. The average time performance of FCTD and SCTPE are 1.17 s and 1.75 s, respectively. Meanwhile, the max time performance of FCTD and SCTPE are 1.75 s and 1.96 s, which are shorter than the time interval of submap input (2 s). The node threads for FCTD

and SCTPE in ROS are illustrated in Fig. 16 and indicate that the proposed FCTD and SCTPE achieve real-time performance.

3.6. Experimental results and accuracy evaluation

Utilizing the proposed method with the parameters according to our experience listed in Table 2, real-time individual tree detection results of the sample plots are illustrated in Fig. 17. From the view inspection of the results of the 9 sample plots, the detected tree trunk positions are close to the ground truth positions, which indicates the effectiveness of the proposed method. A video for the real-time forest inventory can be found in the Appendix video.

The real-time detected individual trees of the selected 9 sample plots using the proposed method are compared with the ground truth data derived from manually measured tree trunk position using TLS.

The individual tree detection results are evaluated and plotted in Table 4. Table 4 indicates that out of 225 reference trees in the 9 sample plots, 219 trees are detected correctly using the proposed method. Overall, the average individual tree detection recall and precision are 0.97 and 0.94, showing the feasibility of the helmet laser scanning system and proposed method in real-time tree detection.

Fig. 18 shows the scatterplot of the estimated parameters and the corresponding ground truth value for all sample plots. The estimated DBH and the ground truth DBH show a high linear relationship

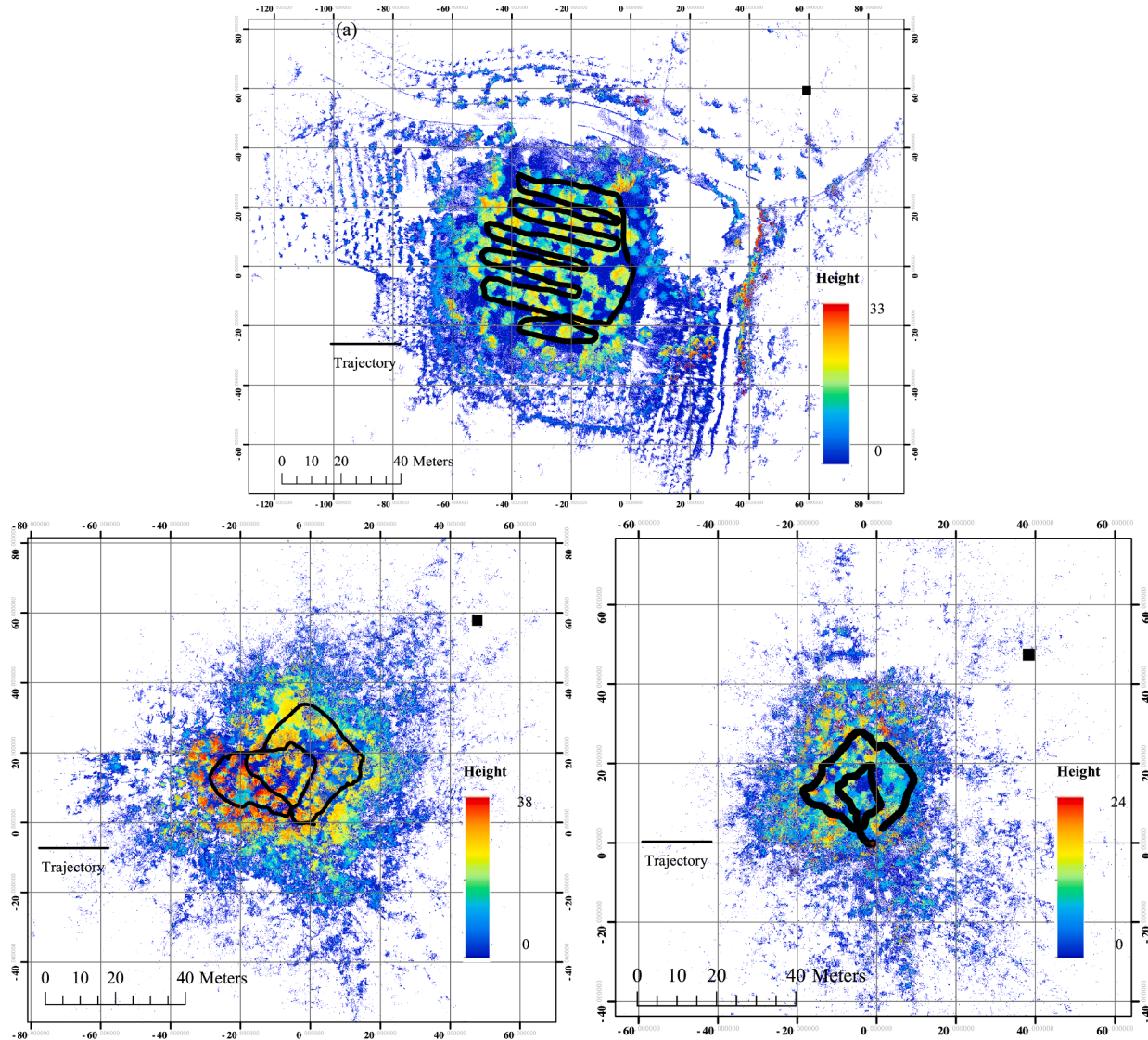


Fig. 12. Point cloud and trajectory collected by the helmet system. (a) Study site 1; (b) Study site 2; (c) Study site 3.

(Pearson's $R = 0.976$). The R^2 and fitting RMSE of the estimated DBH are 0.954 and 0.038 m, respectively. The average DBH error is 0.033 m. The estimated tree height and the tree height show a high linear relationship (Pearson's $R = 0.997$). The R^2 and fitting RMSE of the estimated tree height are 0.997 and 0.294 m, respectively. The average tree height error is 0.231 m. The above evaluation results indicate that the proposed method could achieve robust and accurate DBH estimation using a helmet laser scanning system in real time.

3.7. Comparison with existing methods

3.7.1. Comparison of different individual tree detection methods

We compare the proposed method with several existing individual tree detection methods: (1) Euclidean clustering used in the handheld inventory system proposed by Proudfit et al. (2022); (2) Hierarchical minimum cut (Yang et al., 2016). Fig. 19 is a visual comparison of different tree detection methods with selected submaps from three study sites. The detection results of the proposed method, Euclidean clustering (Proudfit et al., 2022), and hierarchical minimum cut (Yang et al., 2016) are shown in the second column, third column, and fourth column of Fig. 19. From the visual comparison, the proposed method and hierarchical minimum cut achieved good detection results.

Table 5 lists the accuracy and time performance of the different

methods evaluated on all data from study site 1, study site 2, and study site 3. The Euclidean clustering-based method achieves real-time performance (average 0.37 s for each submap) but is error-prone ($recall = 0.66$, $precision = 0.68$) in the dense forest. Because it is only suited for the bare forest, where large space exists between different tree trunks. The dense branches and leaves make it hard to separate different overlapped tree points simply using a distance threshold. The hierarchical minimum cut is a well-known tree detection method and achieves good results ($recall = 0.94$, $precision = 0.95$) but costs too much computation resource (average 17.58 s for each submap). Our method balances time performance (average 1.17 s for each submap) and accuracy ($recall = 0.97$, $precision = 0.94$).

3.7.2. Comparison of different DBH estimation methods

We compare the proposed method with several existing strategies: (1) Estimate the DBH only once when first observing the tree. (2) Update the tree parameter with the one-circle model (Cabo et al., 2018; Pueschel et al., 2013). The different methods are evaluated on all three study sites. The DBH estimation error and processing time are listed in Table 6, which indicates that the one-circle model may result in a large DBH estimation error (average DBH error is 0.068 m, RMSE is 0.073 m), due to the noise of point cloud resulted by the drift of SLAM. Estimating the DBH once using the current submap also results in a large DBH error

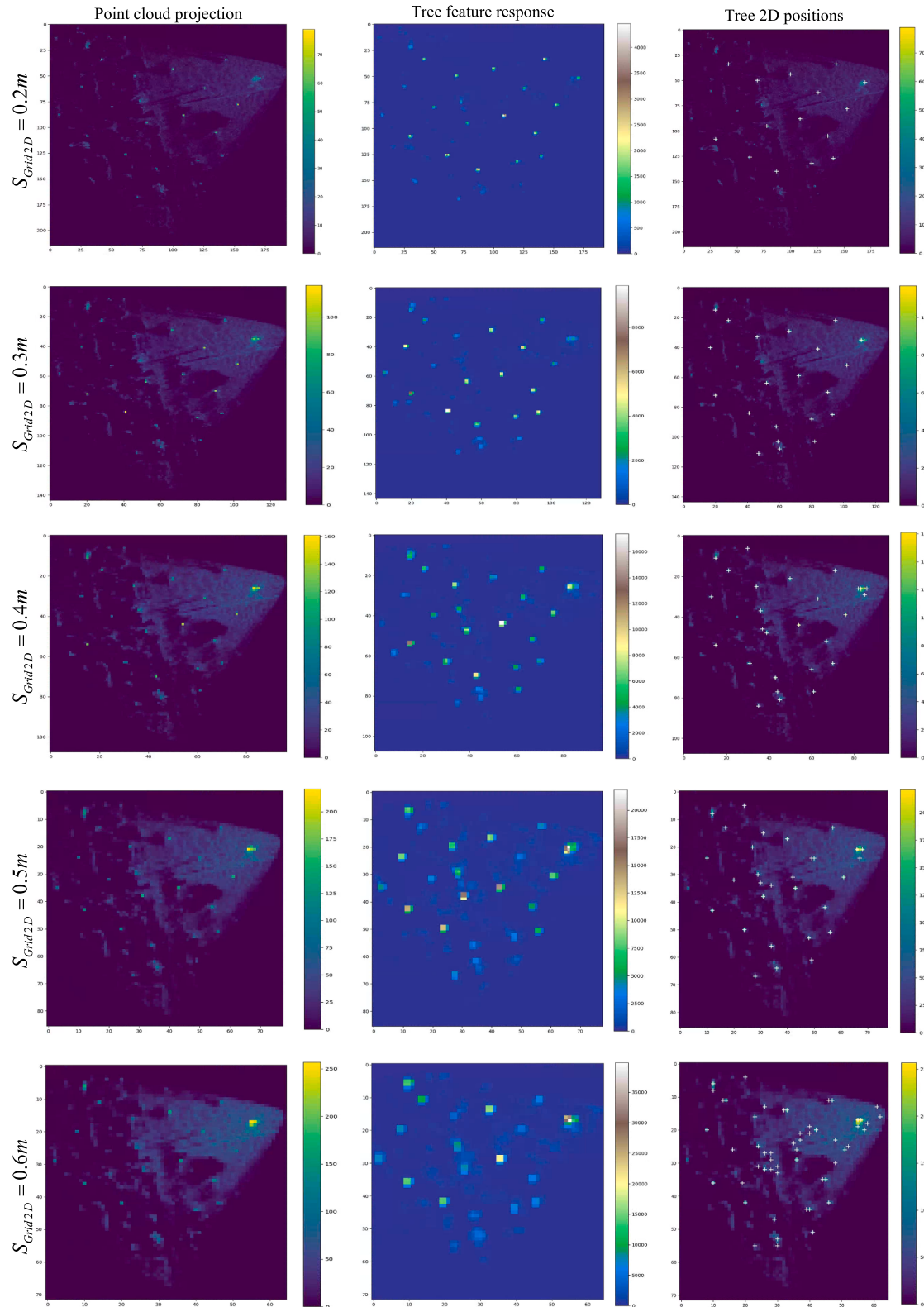


Fig. 13. Intermediate results of tree feature response and detection results using different 2D grid size S_{Grid2D} with fine-tuned Eigen value judgment criteria λ_{min} .

(average DBH error is 0.048 m, RMSE is 0.052 m). The proposed method achieved the best performance (average DBH error is 0.033 m, RMSE is 0.038 m), due to the incomplete scanning data in the current submap. The above results indicate that the proposed method considering the current and existing point cloud submaps achieves better results than the existing one-circle fitting model.

4. Discussion

4.1. Study of real-time performance

In the proposed helmet system, a solid-state LiDAR, LiVOX AVIA with $70.4^\circ \times 77.2^\circ$ field of view, is used. Currently, the LiVOX AVIA is

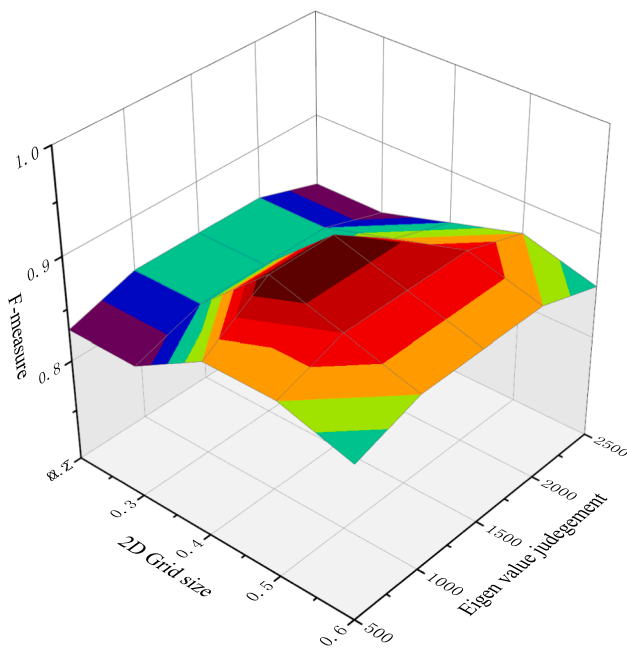


Fig. 14. Parameter-sensitive analysis of 2D grid size S_{Grid2D} and Eigen value judgment criteria λ_{min} in sample plot 1.

one of the most cost-effective solid-state LiDAR, thus it is selected to be integrated into the system. With the fast development and extensive use of solid-state LiDAR, more powerful solid-state LiDAR with a wider field-of-view and longer sensing range will be used in the future. The wider field-of-view and longer range of view, the greater number of points will be in one submap, which may cause more processing time for the tree

detection. Thus in this section, we generate the virtual submap by duplicating the raw submap times as shown in Fig. 20 (a) and (b).

The proposed FCTD and SCTPE are performed using the virtual submaps. Then, the average processing time with respect to the number of trees in one submap are counted and plotted in Fig. 20 (c). From Fig. 20 (c), it could be found that when the number of trees in a submap is lower than 25, the processing times for FCTD and SCTPE are lower than 2 s, which could achieve real-time performance. However, the processing times of point cloud projection in FCTD and RANSAC in

Table 2
Parameter settings.

Parameter	Influence on results	Setting
2D grid size	Determine the resolution of the point cloud projection	$S_{Grid2D} = 0.4m$
Eigen value judgment criteria	Determine the criteria for indicating a corner point on 2D projection	$\lambda_{min} = 1000$
Radius for ground calculation	Determine the smoothness of the DEM.	$S_{NeighborGround} = 2m$
Radius of non-maximum suppression	Identify the maximum value within a certain range to select the best trunk position	$S_{NeighborResponse} = 1m$
Min point density	Screen the 2D grid with too few point projections for effective detection	$I_{min} = 100$

Table 3
Time performance of the proposed method for each point cloud submap.

	Time performance of FCTD (s)			Time performance of SCTPE (s)		
	Min	Max	Average	Min	Max	Average
Study site 1	0.49	1.32	1.21	0.64	1.91	1.69
Study site 2	0.72	1.75	1.10	0.56	1.87	1.75
Study site 3	0.54	1.55	1.19	0.61	1.96	1.81
Overall	0.49	1.75	1.17	0.56	1.96	1.75

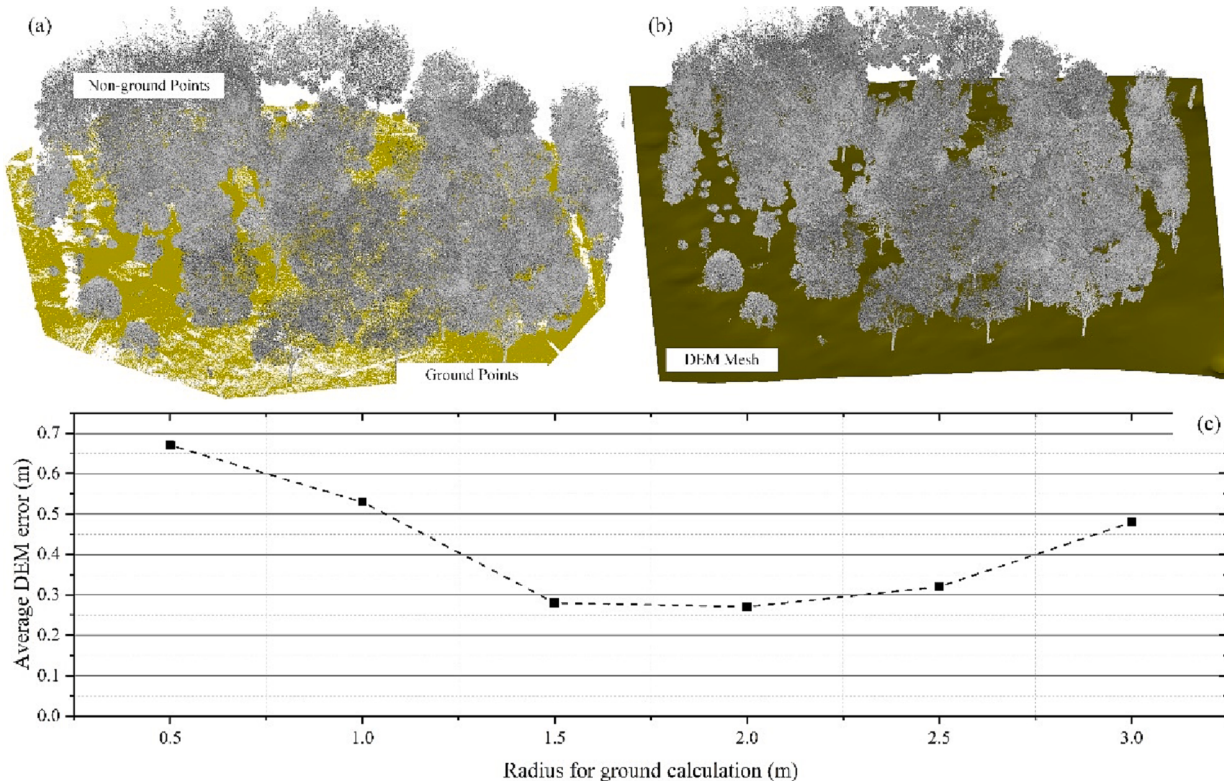


Fig. 15. Parameter sensitive analysis of radius for ground calculation $S_{NeighborGround}$ in sample plot 1. (a) Digital elevation model (DEM) extraction using cloth simulation filtering (CSF). (b) The generated DEM mesh for evaluation. (c) Analysis of DEM error with different $S_{NeighborGround}$ settings.

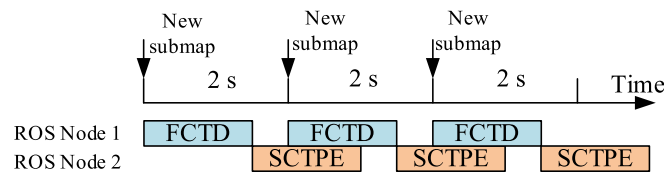


Fig. 16. Illustration of node threads for FCTD and SCTPE in robot operating system (ROS).

SCTPE are both related to the number of trees. When the number of trees in a submap is higher than 25, our system can not achieve real-time performance. The paralleled tree detection and RANSAC will be developed in the future to speed up the processing to meet the requirement for the solid-state LiDAR with a larger field of view.

4.2. Limitation and future works

The RMSE of the tree height is 0.294 m, which is still at a low accuracy level. The large error of the tree height is mainly resulted from

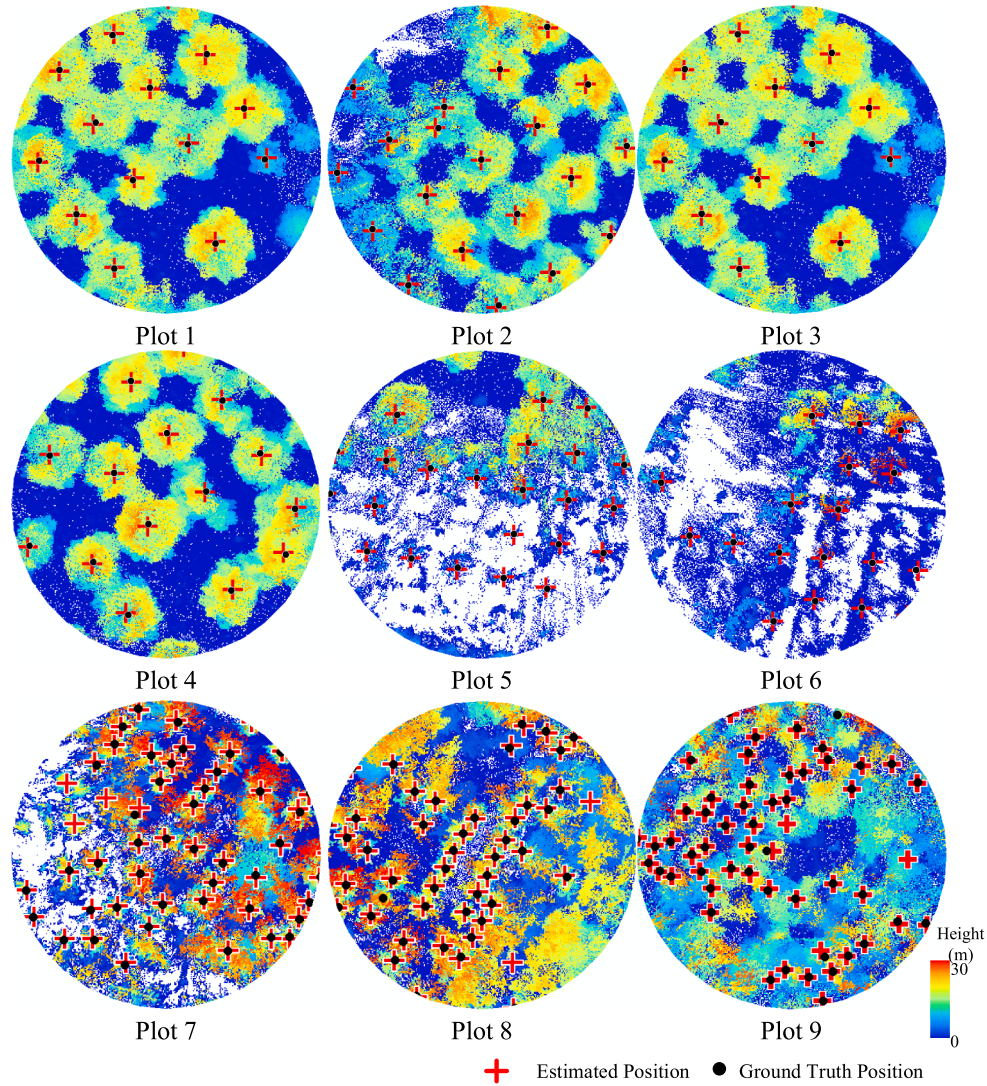


Fig. 17. Real-time individual tree detection results of the sample plots.

Table 4
Evaluation of real-time individual tree detection.

Sample plot ID	Reference Trees	Detected Trees	TP	FN	FP	Recall	Precision	F-measure
1	17	18	16	1	2	0.94	0.89	0.91
2	19	20	18	1	2	0.94	0.90	0.92
3	12	12	11	1	1	0.92	0.92	0.92
4	13	13	13	0	0	1.00	1.00	1.00
5	20	20	20	0	0	1.00	1.00	1.00
6	16	16	16	0	0	1.00	1.00	1.00
7	40	44	39	1	4	0.97	0.91	0.94
8	39	41	38	1	2	0.97	0.95	0.96
9	49	52	48	1	3	0.98	0.94	0.96
Overall	225	236	219	6	14	0.97	0.94	0.96

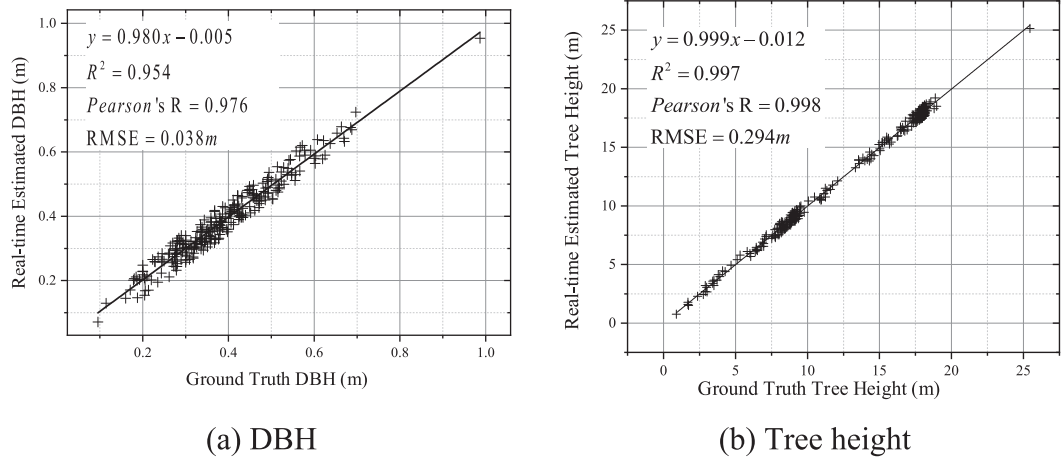


Fig. 18. Scatterplots of tree parameters from real-time estimation and ground-truth for all sample plots.

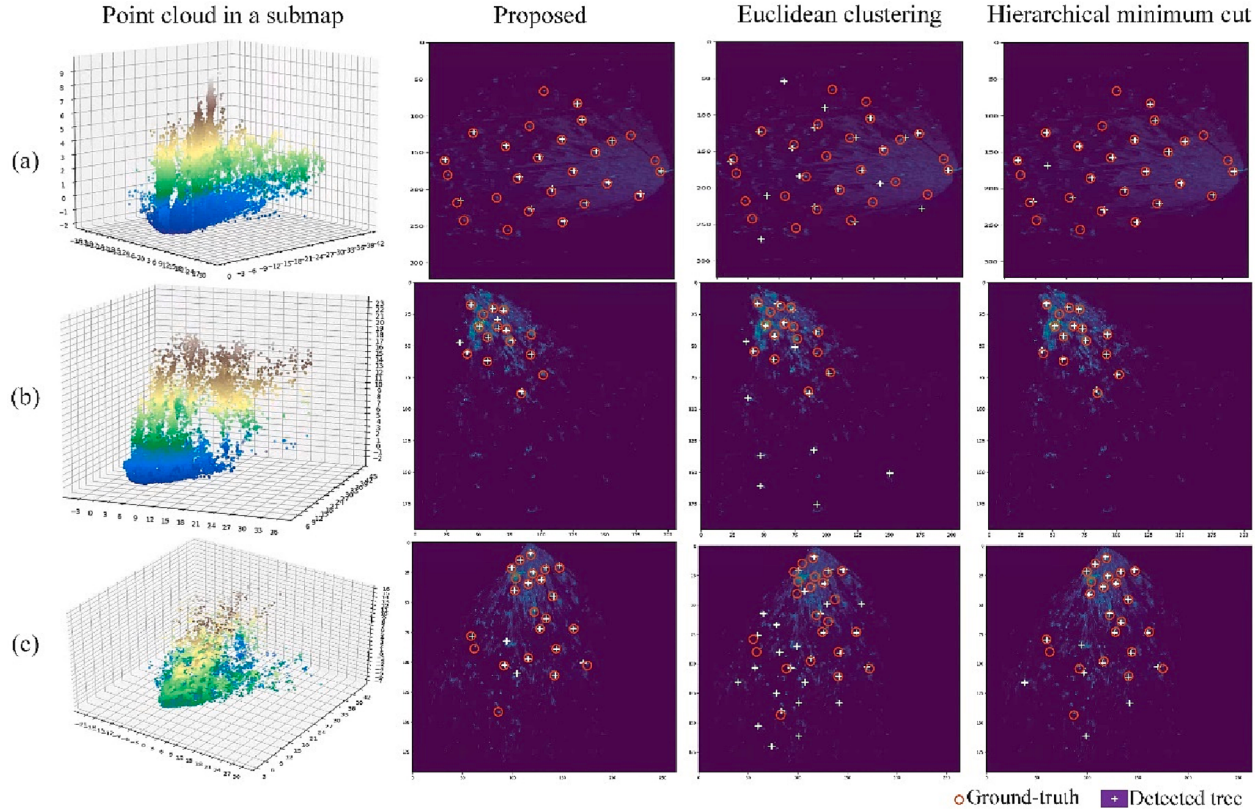


Fig. 19. Visual comparison of different tree detection methods. (a) Randomly selected point cloud submaps in study site 1. (b) Randomly selected point cloud submaps in study site 2. (c) Randomly selected point cloud submaps in study site 3.

Table 5

Comparison of different tree detection methods.

	Proposed method			Euclidean clustering			Hierarchical minimum cut		
	Recall	Precision	Time (s)	Recall	Precision	Time (s)	Recall	Precision	Time (s)
Study site 1	0.97	0.95	1.21	0.64	0.70	0.42	0.97	0.96	17.51
Study site 2	0.97	0.93	1.10	0.65	0.59	0.36	0.93	0.94	17.43
Study site 3	0.98	0.94	1.19	0.71	0.61	0.37	0.90	0.94	18.21
Overall	0.97	0.94	1.17	0.66	0.68	0.37	0.94	0.95	17.58

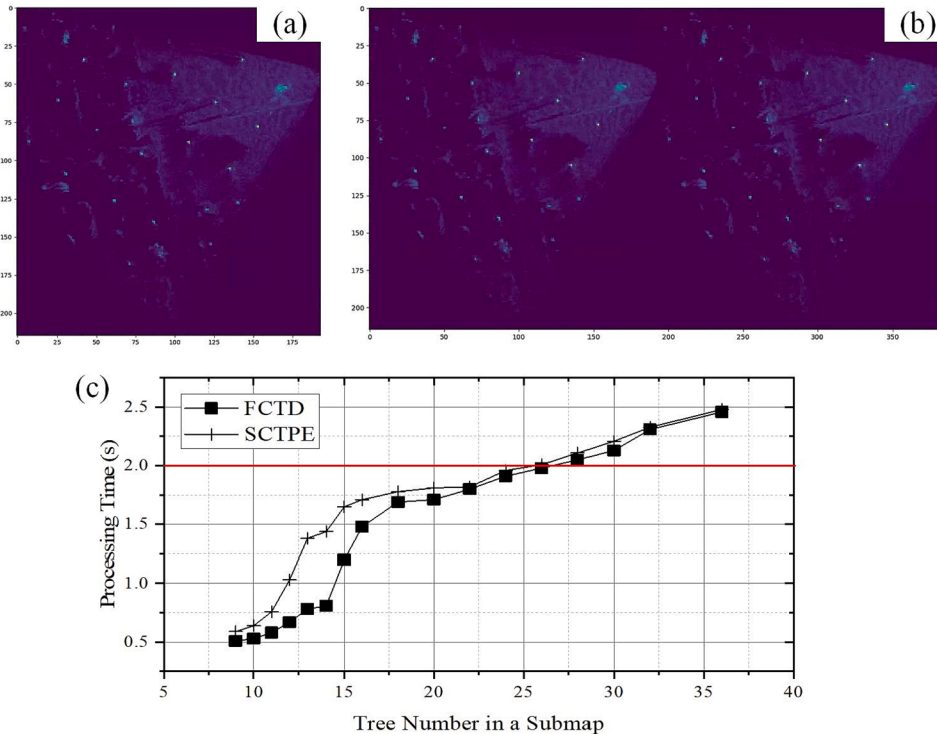
two aspects. The first one is the limited field of view ($70.4^\circ \times 77.2^\circ$) of the LiVOX AVIA LiDAR integrated into the system. The operator may miss the point cloud at the top of the tree as shown in the red rectangle of Fig. 21 (a). The second one is that the wavelength of the LiVOX AVIA

LiDAR is 905 nm, which has limited penetrability compared with the TLS with a wavelength of 1550 nm. With the rapid development of the solid-state LiDAR, there are existing low-cost solid-state LiDAR with a wider range of view and 1550 nm wavelength (e.g., the LS-2 from

Table 6

DBH estimation error and processing time using different methods.

	Proposed method			Estimate once			Update with one-circle model		
	Ave (m)	RMSE (m)	Time (s)	Ave (m)	RMSE (m)	Time (s)	Ave (m)	RMSE (m)	Time (s)
Study site 1	0.031	0.037	1.69	0.041	0.047	1.01	0.066	0.069	1.31
Study site 2	0.035	0.039	1.75	0.046	0.049	1.15	0.068	0.073	1.14
Study site 3	0.034	0.033	1.81	0.051	0.058	1.11	0.071	0.078	1.21
Overall	0.033	0.038	1.75	0.048	0.052	1.09	0.068	0.073	1.25

**Fig. 20.** Study of real-time performance by duplicating the raw submap. (a) The sample raw submap. (b) The sample virtual submap by duplicating the raw submap two times. (c) Processing time.

LSLIDAR²). Thus, we will test the newly released solid-state LiDAR and integrate it into our helmet system to increase the 3D sensing ability of the system.

With the detection strategy of the FCTD, we did not consider the non-tree object in the field sample yet for real-time performance. For example, the non-tree object as shown in Fig. 21 (b) will cause the false detection of the individual tree. Safaei et al. (2021) detect the tree trunks by introducing the Hough transform and active contours. But the process of generating a lot of raster images is time-consuming for the edge-computing unit. To handle the non-tree object problem, López Serrano et al. (2022) propose artificial intelligence-based software (AID-FOREST) for tree detection, where Faster-RCNN (Ren et al., 2015) is used to detect and classify the correct tree object. Inspired by López Serrano et al. (2022), more data and samples will be collected using our helmet system and used for training a tree detection neural network using the SOTA 2D light-weight detection network (e.g., YOLO (Redmon and Farhadi, 2018)) as the backbone to increase the performance of the FCTD.

The tree branch at the breast height as shown in Fig. 21 (c), may result in inaccurate DBH estimation using the proposed SCTPE. In the proposed SCTPE, we only extract three sections at 1.3 m, 1.5 m, and 1.7 m to guarantee real-time performance while eliminating the false tree

candidates from FCTD. López Serrano et al. (2022) extract many cross sections at different tree heights and interpolate the DBH if there is a tree branch. However, more cross sections will lead to a large processing time for the RANSAC algorithm used in the proposed SCTPE. To solve this problem resulted from the tree branch, we will try to develop the parallelized version of the proposed method and extract more sections at different tree heights to increase the robustness while keeping real-time performance.

While the proposed compact helmet system offers a cost-effective solution, users who prioritize data collection efficiency may prefer a backpack system that incorporates multiple scanners or a rotating system, like GeoSLAM. In the future, the proposed method will be extended to backpack systems to achieve a wider field of view and improved efficiency.

5. Conclusion

The paper presents a method for real-time automated forest field inventory using a compact helmet-based laser scanning system. The proposed method consists of two parts: Fast Candidate Tree Detection (FCTD) and Spatiotemporal Consistency-based Tree Parameter Estimation (SCTPE). The FCTD uses a novel 2D corner detection approach to identify the candidate trunk positions from the point cloud submap, while SCTPE uses spatial consistency validation and temporal consistency-based parameter update to estimate the tree parameters.

² <https://www.lslidar.com/product/ls-s2-1550nm-lidar/>.

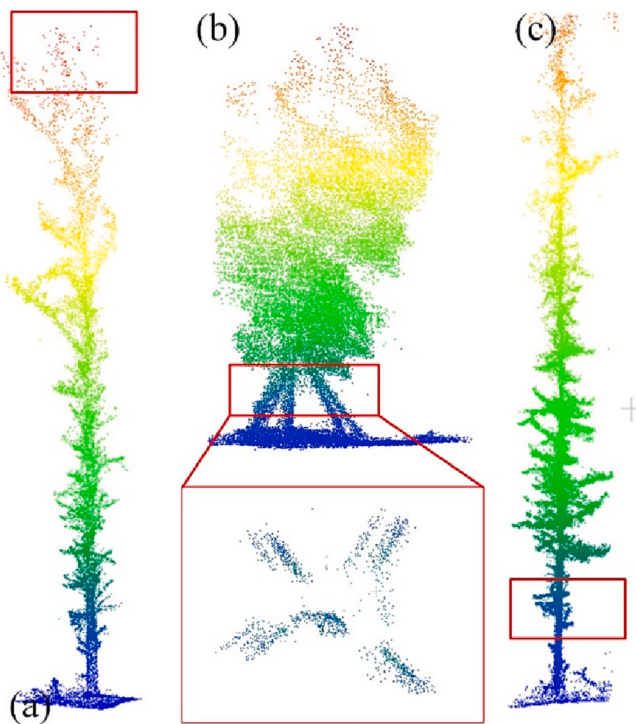


Fig. 21. Limitation analysis of the proposed system. (a) Too sparse or missing point cloud captured by the helmet system at the top of the tree. (b) Non-tree object in the red rectangle. (c) Branch at the breast height of the tree. (For interpretation of the references to color in this figure legend, the reader is referred to the web version of this article.)

The experiments show that the proposed method has a high potential for real-time forest field inventory, with a tree detection accuracy of 96%, average DBH error of 0.05 m, and tree height error of 0.3 m.

However, there is still room for improvement in both hardware and software aspects. In terms of hardware, integrating solid-state LiDAR with a wider field of view and stronger penetration ability can enhance the system's performance. On the software side, future research should consider more complex datasets collected by the helmet system that may not only contain the trees. Leveraging a lightweight neural network trained using the data collected by the helmet and developing a parallelized version of the proposed method may lead to increased robustness while keeping the real-time performance.

CRediT authorship contribution statement

Jianping Li: Conceptualization, Methodology, Writing – original draft, Funding acquisition. **Bisheng Yang:** Writing – review & editing, Funding acquisition, Supervision. **Yandi Yang:** Validation. **Xin Zhao:** Validation. **Youqi Liao:** Validation. **Ningning Zhu:** Writing – review & editing. **Wenxia Dai:** Writing – review & editing. **Rundong Liu:** Writing – review & editing. **Ruibo Chen:** Writing – review & editing. **Zhen Dong:** Writing – review & editing.

Declaration of Competing Interest

The authors declare that they have no known competing financial interests or personal relationships that could have appeared to influence the work reported in this paper.

Data availability

The authors do not have permission to share data.

Acknowledgments

This study was jointly supported by the National Natural Science Foundation Project (No. 42130105, No. 42201477), the National Science Fund for Distinguished Young Scholars (No. 41725005), and China Postdoctoral Science Foundation (2022M712441, 2022TQ0234).

Appendix A. Supplementary data

Supplementary data to this article can be found online at <https://doi.org/10.1016/j.jag.2023.103299>.

References

- Behley, J., Milioto, A., Stachniss, C., 2021. A Benchmark for LiDAR-based Panoptic Segmentation based on KITTI, 2021 IEEE Int Conf Robot Autom. IEEE 13596–13603.
- Bienert, A., Georgi, L., Kunz, M., Maas, H.-G., Von Oheimb, G., 2018. Comparison and combination of mobile and terrestrial laser scanning for natural forest inventories. Forests 9, 395.
- Cabo, C., Del Pozo, S., Rodríguez-González, P., Ordóñez, C., González-Aguilera, D., 2018. Comparing terrestrial laser scanning (TLS) and wearable laser scanning (WLS) for individual tree modeling at plot level. REMOTE SENS-BASEL 10, 540.
- Chen, S.W., Nardari, G.V., Lee, E.S., Qu, C., Liu, X., Romero, R.A.F., Kumar, V., 2020. Sloam: Semantic lidar odometry and mapping for forest inventory. IEEE Robot Autom Lett. 5, 612–619.
- Chudá, J., Hunčák, M., Tuček, J., Mokroš, M., 2020. The handheld mobile laser scanners as a tool for accurate positioning under forest canopy. The International Archives of Photogrammetry, Remote Sensing and Spatial Information Sciences 43, 211–218.
- Dai, W., Yang, B., Dong, Z., Shaker, A., 2018. A new method for 3D individual tree extraction using multispectral airborne LiDAR point clouds. ISPRS J Photogramm Remote Sens. 144, 400–411.
- de Miguel-Díez, F., Reder, S., Wallor, E., Bahr, H., Blasko, L., Mund, J.-P., Cremer, T., 2022. Further application of using a personal laser scanner and simultaneous localization and mapping technology to estimate the log's volume and its comparison with traditional methods. Int J Appl Earth Obs Geoinf. 109, 102779.
- Derpanis, K.G., 2010. Overview of the RANSAC Algorithm. Image Rochester NY 4, 2–3.
- Dong, Z., Liang, F., Yang, B., Xu, Y., Zang, Y., Li, J., Wang, Y., Dai, W., Fan, H., Hyppä, J., 2020. Registration of large-scale terrestrial laser scanner point clouds: A review and benchmark. ISPRS J Photogramm Remote Sens. 163, 327–342.
- Fan, Y., Feng, Z., Shen, C., Khan, T.U., Mannan, A., Gao, X., Chen, P., Saeed, S., 2020. A trunk-based SLAM backend for smartphones with online SLAM in large-scale forest inventories. ISPRS J Photogramm Remote Sens. 162, 41–49.
- GIMInternational, 2021. Capturing the environment with a lidar equipped helmet. <https://www.gim-international.com/content/news/capturing-the-environment-with-a-lidar-equipped-helmet>.
- Hsiao, P.-Y., Lu, C.-L., Fu, L.-C., 2010. Multilayered image processing for multiscale Harris corner detection in digital realization. IEEE Trans Ind Electron. 57, 1799–1805.
- Hyppä, E., Hyppä, J., Hakala, T., Kukko, A., Wulder, M.A., White, J.C., Pyörälä, J., Yu, X., Wang, Y., Virtanen, J.-P., 2020. Under-canopy UAV laser scanning for accurate forest field measurements. ISPRS J Photogramm Remote Sens. 164, 41–60.
- Kükenbrink, D., Marty, M., Bösch, R., Ginzler, C., 2022. Benchmarking laser scanning and terrestrial photogrammetry to extract forest inventory parameters in a complex temperate forest. Int J Appl Earth Obs Geoinf. 113, 102999.
- Kukko, A., Kaijaluoto, R., Kaartinen, H., Lehtola, V.V., Jaakkola, A., Hyppä, J., 2017. Graph SLAM correction for single scanner MLS forest data under boreal forest canopy. ISPRS J Photogramm Remote Sens. 132, 199–209.
- Kuželka, K., Marušák, R., Surový, P., 2022. Inventory of close-to-nature forest stands using terrestrial mobile laser scanning. Int J Appl Earth Obs Geoinf. 115, 103104.
- Lei, X., Tang, M., Lu, Y., Hong, L., Tian, D., 2009. Forest inventory in China: status and challenges. INT FOREST REV. 11, 52–63.
- Li, J., Yang, B., Chen, C., Habib, A., 2019. NRRI-UAV: Non-rigid registration of sequential raw laser scans and images for low-cost UAV LiDAR point cloud quality improvement. ISPRS J Photogramm Remote Sens. 158, 123–145.
- Li, J., Yang, B., Chen, Y., Wu, W., Yang, Y., Zhao, X., Chen, R., 2022. EVALUATION OF A COMPACT HELMET-BASED LASER SCANNING SYSTEM FOR ABOVEGROUND AND UNDERGROUND 3D MAPPING. The International Archives of Photogrammetry, Remote Sensing Spatial Information Sciences 43, 215–220.
- Liang, X., Hyppä, J., Kaartinen, H., Lehtomäki, M., Pyörälä, J., Pfeifer, N., Holopainen, M., Broly, G., Francesco, P., Hackenberg, J., 2018a. International benchmarking of terrestrial laser scanning approaches for forest inventories. ISPRS J Photogramm Remote Sens. 144, 137–179.
- Liang, X., Kankare, V., Hyppä, J., Wang, Y., Kukko, A., Haggrén, H., Yu, X., Kaartinen, H., Jaakkola, A., Wang, Y., 2018b. In-situ measurements from mobile platforms: An emerging approach to address the old challenges associated with forest inventories. ISPRS J Photogramm Remote Sens. 143, 97–107.
- Liu, K., Shen, X., Cao, L., Wang, G., Cao, F., 2018. Estimating forest structural attributes using UAV-LiDAR data in Ginkgo plantations. ISPRS J Photogramm Remote Sens. 146, 465–482.

- livoxtech, 2023. mainpage of livox avia. <https://www.livoxtech.com/avia>.
- López Serrano, F.R., Rubio, E., García Morote, F.A., Andrés Abellán, M., Picazo Córdoba, M.I., García Saucedo, F., Martínez García, E., Sánchez García, J.M., Serena Innerarity, J., Carrasco Lucas, L., García González, O., García González, J.C., 2022. Artificial intelligence-based software (AID-FOREST) for tree detection: A new framework for fast and accurate forest inventorying using LiDAR point clouds. *Int J Appl Earth Obs Geoinf.* 113, 103014.
- Mokroš, M., Mikita, T., Singh, A., Tomašík, J., Chudá, J., Wężyk, P., Kuželka, K., Surový, P., Klímanek, M., Zięba-Kulawik, K., 2021. Novel low-cost mobile mapping systems for forest inventories as terrestrial laser scanning alternatives. *Int J Appl Earth Obs Geoinf.* 104, 102512.
- Näyhä, A., 2019. Transition in the Finnish forest-based sector: Company perspectives on the bioeconomy, circular economy and sustainability. *J. CLEAN PROD.* 209, 1294–1306.
- Pierzchala, M., Giguère, P., Astrup, R., 2018. Mapping forests using an unmanned ground vehicle with 3D LiDAR and graph-SLAM. *Comput Electron Agric.* 145, 217–225.
- Point2Model, 2023. Point2Model. <http://www.dynspai.com/cpfw>.
- Powers, D.M., 2020. Evaluation: from precision, recall and F-measure to ROC, informedness, markedness and correlation. *arXiv preprint arXiv:16061*.
- Proudman, A., Ramezani, M., Digumarti, S.T., Chebrolu, N., Fallon, M., 2022. Towards real-time forest inventory using handheld LiDAR. *ROBOT AUTON. SYST.* 157, 104240.
- Pueschel, P., Newnham, G., Rock, G., Udelhoven, T., Werner, W., Hill, J., 2013. The influence of scan mode and circle fitting on tree stem detection, stem diameter and volume extraction from terrestrial laser scans. *ISPRS J Photogramm Remote Sens.* 77, 44–56.
- Qian, C., Liu, H., Tang, J., Chen, Y., Kaartinen, H., Kukko, A., Zhu, L., Liang, X., Chen, L., Hyppä, J., 2016. An integrated GNSS/INS/LiDAR-SLAM positioning method for highly accurate forest stem mapping. *REMOTE SENS-BASEL* 9, 3.
- Redmon, J., Farhadi, A., 2018. Yolov3: An incremental improvement. *arXiv preprint arXiv:02767*.
- Ren, S., He, K., Girshick, R., Sun, J., 2015. Faster r-cnn: Towards real-time object detection with region proposal networks. *Adv Neural Inf Process Syst.* 28.
- Safaie, A.H., Rastiveis, H., Shams, A., Sarasua, W.A., Li, J., 2021. Automated street tree inventory using mobile LiDAR point clouds based on Hough transform and active contours. *ISPRS J Photogramm Remote Sens.* 174, 19–34.
- Su, Y., Guo, Q., Jin, S., Guan, H., Sun, X., Ma, Q., Hu, T., Wang, R., Li, Y., 2020. The development and evaluation of a backpack LiDAR system for accurate and efficient forest inventory. *IEEE Geosci Remote Sens Lett.* 18, 1660–1664.
- Wang, L., Jia, M., Yin, D., Tian, J., 2019. A review of remote sensing for mangrove forests: 1956–2018. *REMOTE SENS. ENVIRON.* 231, 111223.
- Xiao, J., Chevallier, F., Gomez, C., Guanter, L., Hicke, J.A., Huete, A.R., Ichii, K., Ni, W., Pang, Y., Rahman, A.F., 2019. Remote sensing of the terrestrial carbon cycle: A review of advances over 50 years. *REMOTE SENS. ENVIRON.* 233, 111383.
- Xu, W., Cai, Y., He, D., Lin, J., Zhang, F., 2022. Fast-lio2: Fast direct lidar-inertial odometry. *IEEE Trans Robot.*
- Yan, F., Ullah, M.R., Gong, Y., Feng, Z., Chowdury, Y., Wu, L., 2012. Use of a no prism total station for field measurements in *Pinus tabulaeformis* Carr. stands in China. *Biosystems engineering* 113, 259–265.
- Yang, B., Dai, W., Dong, Z., Liu, Y., 2016. Automatic forest mapping at individual tree levels from terrestrial laser scanning point clouds with a hierarchical minimum cut method. *REMOTE SENS-BASEL* 8, 372.
- Yang, B., Li, J., 2022. A hierarchical approach for refining point cloud quality of a low cost UAV LiDAR system in the urban environment. *ISPRS J Photogramm Remote Sens.* 183, 403–421.
- Zhang, W., Qi, J., Wan, P., Wang, H., Xie, D., Wang, X., Yan, G., 2016. An easy-to-use airborne LiDAR data filtering method based on cloth simulation. *REMOTE SENS-BASEL* 8, 501.
- Zhu, Z., Lin, K., Zhou, J., 2020. Transfer learning in deep reinforcement learning: A survey. *arXiv preprint arXiv:2009.07888*.